Measurement of the Low-Energy Electron Inelastic Mean Free Path in Monolayer Graphene

Bo Da, Yang Sun, Zhufeng Hou, Jiangwei Liu, Nguyen Thanh Cuong, Kazuhito Tsukagoshi, Hideki Yoshikawa, Shigeo Tanuma, Jin Hu, Zhaoshun Gao, and Zejun Ding

Phys. Rev. Applied **13**, 044055 — Published 21 April 2020

DOI: 10.1103/PhysRevApplied.13.044055

Measurement of the low-energy electron inelastic mean free path in monolayer graphene

Bo Da[1,2*], Yang Sun[3], Zhufeng Hou[1], Jiangwei Liu[4], Nguyen Thanh Cuong[5,6], Kazuhito Tsukagoshi[6], Hideki Yoshikawa[1,2†], Shigeo Tanuma[2], Jin Hu[7], Zhaoshun Gao[8] & Zejun Ding[9‡]

[1]Research and Services Division of Materials Data and Integrated System, National Institute for Materials Science, 1-1 Namiki, Tsukuba, Ibaraki 305-0044, Japan.

[2]Research Center for Advanced Measurement and Characterization, National Institute for Materials Science, 1-2-1 Sengen, Tsukuba, Ibaraki 305-0047, Japan.

[3]Department of Applied Physics and Applied Mathematics, Columbia University, New York, NY, 10027, USA.

[4]Research Center for Functional Materials, National Institute for Materials Science, 1-2-1 Sengen, Tsukuba, Ibaraki 305-0047, Japan.

[5]International Center for Young Scientists (ICYS), National Institute for Materials Science, Tsukuba, Ibaraki 305-0044, Japan.

[6]International Center for Materials Nanoarchitectonics (WPI-MANA), National Institute for Materials Science, Tsukuba, Ibaraki 305-0044, Japan.

[7]Department of Physics and Institute for Nanoscience and Engineering, University of Arkansas, Fayetteville, Arkansas 72701, USA.

[8]Institute of Electrical Engineering, Chinese Academy of Sciences, Beijing, 100190, P.R. China.

[9]Department of Physics, University of Science and Technology of China, Hefei, Auhui 230026, P.R. China.

[*]DA.Bo@nims.go.jp

[†]YOSHIKAWA.Hideki@nims.go.jp

[‡]Zjding@ustc.edu.cn

Abstract:

Measuring electron transport properties of substrate-supported nanomaterials with the traditional two-point comparison method is difficult at electron energies below 50 eV, where core-level signals are too feeble to be detected against the strong secondary-electron background. Herein, a data-driven spectral analysis technique is used to study the low-energy electron transport properties of substrate-supported target nanomaterials while eliminating the influence from the substrate signal. Applying this technique, the electron transport properties of the effective attenuation length and the inelastic mean free path (IMFP) can be determined with extremely high efficiency over the entire measured energy range of 6–600 eV. Further, these results show excellent agreement with other experimental and theoretical results. Significant differences are observed between monolayer graphene and bulk graphite IMFP, which illustrates the importance of the nanometer effect in the electron transport properties of the material. Furthermore, this technique is readily applicable to any ultrathin material that can be transferred onto a polycrystalline gold substrate.

1. Introduction

Surface analysis techniques such as x-ray photoelectron spectroscopy (XPS) and Auger electron spectroscopy (AES) are widely used for a broad range of materials, and provide quantitative elemental and chemical state information from the surface of the material being studied [*1–4*]. Nowadays, these techniques are intensively employed to study nanomaterials and focus on a sole target, mapping the surface elemental composition of nanomaterial [*5–6*]. However, the capabilities of these techniques to play a greater role in nanomaterial studies are limited owing to the lack of quantitative knowledge of electron transport properties in the target nanomaterials. Although knowing that the transport properties of nanomaterials must differ from those of its

corresponding allotrope in bulk form, physicists working in surface analysis still try to analyze the measured spectra of nanomaterials using its bulk form parameters. Obviously, the information obtained thereby is built upon a false premise, making it unreliable for providing even qualitative information, let alone quantitative information. Even for the most straightforward application of mapping the surface elemental composition of a nanomaterial, the exact depth from which these elemental compositions were obtained is generally unknown. The situation is even worse when studying substrate-supported nanomaterials using any electron-beam techniques that employ low-energy electrons (generally below 50 eV) as information carriers because of the ineluctable disturbance of secondary electron (SE) signals from both the covering nanomaterial and underlying substrate. For instance, we have no idea whether the scanning electron microscope image of a substrate-supported nanomaterial sample displays the nanomaterial itself or the morphology of the substrate beneath the nanomaterial. Undisputedly, this lack of quantitative information concerning the electron transport properties of nanomaterials has significantly blocked the way for further development of nanomaterial study using electron beam techniques. This is especially true for techniques involving low-energy electrons such as next-generation energy-filtered SE microscopy with improved energy resolution [*7*].

Electron transport properties are generally quantified by the inelastic mean free path (IMFP) of electrons [*8*], which characterizes the average distance that an electron travels through a solid before losing energy. Much effort has been devoted to measuring the IMFPs of electrons in various materials, generally at kiloelectronvolt-scale energies, using elastic peak electron spectroscopy (EPES) combined with a corresponding Monte Carlo (MC) simulation [*9–11*]. Recently, X-ray absorption fine structure techniques have been used to determine the IMFPs of

bulk materials at electron energies (*E*) below 120 eV by comparison with a theoretical prediction [*12*]. However, these two techniques developed for bulk materials cannot be extended to nanofilm samples. The low-energy electron reflectivity from a nanofilm has been used to extract the IMFP of Fe in the energy range from 4 to 18 eV from an Fe film on W(110) [*13*]. However, such a measurement is difficult to apply to a graphene sample and/or to a wider energy range, because considerable prior knowledge of both the nanofilm and substrate is required.

In addition to the IMFP, an experimentally defined quantification of the electron transport properties that includes the contribution of elastic scattering to their trajectories is given by the effective attenuation length (EAL) [*14*]. EAL is generally determined using the so-called overlayer method [*15*] from changes in the AES or XPS core-level signal intensities for overlayer films of various thicknesses deposited on a substrate. A large number of EAL measurements [*14*,*16*,*17*] have been obtained for thin films of various materials with thicknesses ranging from a few nanometres to tens of nanometres at the core-level energies of substrates. However, even using a synchrotron radiation source, this technique does not work at energies below 15 eV, where the core-level signals from the substrate are overwhelmed by the strong secondary electron (SE) background in AES and XPS measurements.

However, in most electron spectroscopic data analyses the SE background signals are neglected as noise and are not quantitatively analyzed. The main reason for this is that the widely used physics-driven spectral analysis approaches on which the analysis is based, describe the measured data in terms of physically meaningful parameters, i.e. physically defined (PD) descriptors designated from an informatics point of view. Therefore, the currently available physics-driven spectral analysis approaches are only able to analyze the peak signal and generally do not make use of the SE background signal owing to the difficulty in modelling

accurate physical mechanisms of SE excitation and emission, despite it being known that the SE background signals must involve quantitative information about the electron transport properties. To extract meaningful information from the SE background signal, a new method is required that is fundamentally different to the conventional physics-driven spectral analysis approaches in which only peak signals can be analyzed.

In this work, we propose a new heuristic data-driven spectral analysis technique to overcome current limitations. Instead of interpreting individual measurements in terms of only PD descriptors, analytically defined (AD) descriptors obtained through the data analysis of many slightly different conditions, are used to describe the background data. These AD descriptors are ranked according to specified scores so that those with high scores may be effective for describing the measurements under slightly different experimental conditions.

In the following section, we demonstrate this new technique using an example that aims to measure the electron transport properties of substrate-supported graphene using the SE background in AES spectra, with no influence from the substrate. The implementation of this method comprises three steps: First, the SE spectra of graphene samples with different thicknesses or on different substrates are measured to accumulate information about graphene (Section 2.1). Then, specific combinations of these measurements, termed analytically defined (AD) descriptors, which have a high graphene information content are sorted from the extensive list of candidates (Section 2.2). Finally, the selected principle AD descriptors are further analyzed using a corresponding physical model to quantitatively reveal the electron transport properties of graphene, as described in Section 2.3. In addition, the correctness of the physical quantities of graphene obtained in this work is verified in Section 3. The reliability of the proposed technique in the energy range 50–600 eV is first verified by comparing the extracted

EAL and IMFP values of graphene with well-established ones obtained theoretically or experimentally and this is described in Section 3.1. The low energy performance of the proposed technique is then discussed in Section 3.2 and Section 3.3, focusing on the low energy electron transmissivity of graphene, and the resulting EAL and IMFP values of graphene, respectively. All of the evidence presented in this work suggests that the proposed method is able to extract reliable electron transport properties for graphene from SE background signal even when the graphene is supported by a substrate.

2. Experimental Methods

2.1. Measurements under slightly different conditions

Because our goal was to extract quantitative information of graphene from SE spectra, the first step was to gather enough SE spectra containing graphene information in different ways. Figure 1a shows a commercial AES setup with a cylindrical mirror analyser (CMA). Focused electrons were incident on the substrate-supported graphene sample and emitted electrons were detected by the CMA to capture SE spectra. A polycrystalline gold (Au) substrate (see Appendix A) was selected to support the target graphene because different types of SE spectra can be measured at different regions of a polycrystalline substrate to accumulate graphene information as a result of its distinct crystallographic orientations. According to the scanning electron microscopy image in the inset of Fig. 1b, four types of SE spectra with sufficient stability and repeatability were measured by selecting incident positions on bright (S_B) and dark (S_D) regions of the bare substrate and similar regions covered by graphene sheets, as illustrated in Fig. 1b. In these SE spectra, broad SE peaks with some weak features as shoulders were observed, which may originate from the coupling of several physical mechanisms including the diffraction effect and

140 characteristic SE emission, and therefore are generally regarded as part of the uninterpreted SE
141 background.
142 Although these four SE spectra measured from different specified regions of the same sample
143 were of suitable quality for use as basic elements to construct candidate AD descriptors, more
144 interrelated SE spectra were needed to implement the proposed data-driven spectral analysis
145 method. Here, two more representative experiment variables were applied to accumulate more
146 graphene information from different aspects; these variables were the energy of the incident
147 electron beam (E_{in}), which was assessed at three levels, i.e., 10 keV (E_{10}), 15 keV (E_{15}), and 20
148 keV (E_{20}), and the layer number of graphene (G_n), for which two levels were considered; i.e.,
149 monolayer graphene (G_1) and bilayer graphene (G_2). Taking into account the two possible
150 incident positions (S_B and S_D), up to 18 different types of SE spectra could be measured from one
151 sample in the energy range of 0–50 eV, as presented in Appendix A. To compare our results with
152 well-established theoretical and experimental approaches that are only available at electron
153 energies (E) above 50 eV, one more group of SE spectra was measured at E of up to 600 eV (see
154 Appendix A). From the viewpoint of mathematics, SE spectra can be interpreted as functions that
155 depend on the selected experimental variables; thereby, the spectra measured for the bare
156 substrate and graphene could be written as $J_{Sub}(E, S_i, E_{in})$ and $J_{Gra}(E, G_n, S_i, E_{in})$, respectively,
157 where S_i represents specific regions on the substrate $S_i \in [S_B, S_D]$. E is omitted below for brevity.

158 **2.2. Determining principle AD descriptors**

159 Based on these SE spectra, candidate AD descriptors for certain combinational math operations
160 of these spectra were randomly constructed with algebra and further defined as a descriptor
161 space. To create an affordable descriptor space, here, the candidate AD descriptors were

162 constructed merely by exhaustively listing all the possible ratios of linear combinations of four
163 SE spectra measured from different specified regions of the same sample, as follows:

164 $$\mathrm{D}\left(\mathbf{a}, G_{\mathrm{n}}, E_{\mathrm{in}}\right)=\frac{a_1 J_{\mathrm{Gra}}\left(G_{\mathrm{n}}, S_{\mathrm{B}}, E_{\mathrm{in}}\right)+a_2 J_{\mathrm{Gra}}\left(G_{\mathrm{n}}, S_{\mathrm{D}}, E_{\mathrm{in}}\right)+a_3 J_{\mathrm{Sub}}\left(S_{\mathrm{B}}, E_{\mathrm{in}}\right)+a_4 J_{\mathrm{Sub}}\left(S_{\mathrm{D}}, E_{\mathrm{in}}\right)}{a_5 J_{\mathrm{Gra}}\left(G_{\mathrm{n}}, S_{\mathrm{B}}, E_{\mathrm{in}}\right)+a_6 J_{\mathrm{Gra}}\left(G_{\mathrm{n}}, S_{\mathrm{D}}, E_{\mathrm{in}}\right)+a_7 J_{\mathrm{Sub}}\left(S_{\mathrm{B}}, E_{\mathrm{in}}\right)+a_8 J_{\mathrm{Sub}}\left(S_{\mathrm{D}}, E_{\mathrm{in}}\right)}; \quad (1)$$

165 where D(**a**, G_{n}, E_{in}) is a candidate AD descriptor as a function of weight factor vector **a**, G_{n}, and
166 E_{in}. The eight components of vector **a** (a_1, a_2, a_3, a_4, a_5, a_6, a_7, and a_8) were used as weight
167 factors to construct candidate descriptors and each component a_{i} was restricted to the value of
168 −1, 0, or 1 for simplicity.

169 The next step involved identifying the AD descriptors with a large percentage of graphene
170 information from the candidates. Clearly, such AD descriptors should be insensitive to the
171 experiment variable that has almost no effect on the proportion of graphene information in the
172 measured spectra, represented by E_{in}, and simultaneously sensitive to any slight changes in the
173 experiment variable that strongly affect the proportion of graphene information in the measured
174 spectra, represented by G_{n}. Therefore, the essence of the selection of requested AD descriptors
175 according to their sensitivities to experiment variables is a typical multi-objective optimization
176 problem, and could be solved by introducing the economic concept of Pareto optimality [*18*].
177 The Pareto optimality describes resource allocation in which reallocation to benefit any one
178 individual or preference criterion is not possible without making at least one individual or
179 preference criterion worse off. Here, the sensitivities of AD descriptors to experimental variables
180 are set as criteria in the presented Pareto optimization process to determine the Pareto optimal
181 descriptors that reach an optimal insensitivity to E_{in} and optimal sensitivity to G_{n} at the same
182 time. To demonstrate such Pareto optimization processes in a more intuitive way, the
183 sensitivities of every candidate descriptor to E_{in} (Score1) and G_{n} (Score2) were calculated using

simple statistical arguments (refer to the Methods section for details) and drawn in a descriptor performance map (Fig. 2a) as the x- and y-axis, respectively. In this map, a set of Pareto optimal descriptors (D_n) that could not be improved in either Score1 or Score2 without degrading the other one was found at the upper-left boundary of all candidate descriptors and numbered in this descriptor performance map in order of increasing Score1. The weight factors **a** of these Pareto optimal descriptors are listed in Table 1.

For comparison, three traditional AD descriptors, i.e. $J_{Gra}(G_n, S_i)/J_{Sub}(S_i)$, $\frac{J_{Gra}(G_n, S_i) - J_{Sub}(S_i)}{J_{Sub}(S_i)}$, and $\frac{J_{Sub}(S_i) - J_{Gra}(G_n, S_i)}{J_{Sub}(S_i) + J_{Gra}(G_n, S_i)}$, are also presented in this map. The first corresponds to the most widely used spectral ratioing technique. It is located in the central area of deleted candidates, which implies that is not an appropriate solution to provide quantitative information on a substrate-supported graphene sample from the collected SE signals. Meanwhile the latter two are located at the upper left boundary of all candidate descriptors, and are D_{28} and D_{33} of the selected Pareto optimal descriptors, respectively. They are the best solutions that were produced completely digitally to extract information on the substrate-supported graphene. Furthermore, D_{28} and D_{33} were used as contrast parameters in Refs. [*19*,*20*], respectively, to quantitatively analyse the incident beam energy-dependence of the SEM contrast of graphene for various layers.

Although every Pareto optimal descriptor has a large percentage of graphene information and can be directly used to characterize graphene as D_{28} and D_{33} descriptors, some of them contain more graphene information than others and can be further identified by their coefficient of variation (c_v). As shown in Fig. 2b, the c_v of these descriptors was calculated to evaluate whether the bias of the Pareto optimal descriptors caused by different G_n was sufficiently large to be

observed under the disturbance of different E_{in} (see the Appendix B for details). A total of 12 Pareto optimal descriptors with c_v smaller than 15% were found in Fig. 2b, but only nine of them were a suitable distance away from the main area of deleted candidates indicated by a blue dashed oval in Fig. 2a. Considering that the distance between two descriptors in Fig. 2a roughly reflects the difference between them, only nine descriptors; (i.e., D_{18}, D_{19}, D_{20}, D_{21}, D_{22}, D_{23}, D_{38}, D_{39}, and D_{40}, see Appendix B for more details) are of the most interest. This is because these descriptors have a larger probability of providing unique graphene information than those located near the main area of deleted candidates. These descriptors are hereafter named the principle AD descriptors.

2.3. Physical picture of principle AD descriptors

The weight factors **a** of the principle AD descriptors are listed in Table 2. Careful inspection revealed that **a** associated with two different substrates (i.e., [a_1, a_2], [a_3, a_4], [a_5, a_6], and [a_7, a_8]) always appeared in the same combination with opposite signs. Therefore, Eqn. 1 can be rewritten as

$$\mathrm{D}_{\mathrm{Principle}}\left(\mathbf{b}, G_{\mathrm{n}}, E_{\mathrm{in}}\right)=\frac{b_1\left[J_{\mathrm{Gra}}\left(G_{\mathrm{n}}, S_{\mathrm{B}}, E_{\mathrm{in}}\right)-J_{\mathrm{Gra}}\left(G_{\mathrm{n}}, S_{\mathrm{D}}, E_{\mathrm{in}}\right)\right]+b_2\left[J_{\mathrm{Sub}}\left(S_{\mathrm{B}}, E_{\mathrm{in}}\right)-J_{\mathrm{Sub}}\left(S_{\mathrm{D}}, E_{\mathrm{in}}\right)\right]}{b_3\left[J_{\mathrm{Gra}}\left(G_{\mathrm{n}}, S_{\mathrm{B}}, E_{\mathrm{in}}\right)-J_{\mathrm{Gra}}\left(G_{\mathrm{n}}, S_{\mathrm{D}}, E_{\mathrm{in}}\right)\right]+b_4\left[J_{\mathrm{Sub}}\left(S_{\mathrm{B}}, E_{\mathrm{in}}\right)-J_{\mathrm{Sub}}\left(S_{\mathrm{D}}, E_{\mathrm{in}}\right)\right]}; \quad (2)$$

where four components of vector **b** = [b_1, b_2, b_3, b_4] are used to replace the eight-component vector **a**, as shown in Table 2. This simplification of Eqn. 1 implies that S_i-independent terms exist in the measured SE spectra that can be offset through the subtraction of one measurement from another for the principle descriptors. According to this reasoning, the SE spectra measured for graphene, $J_{Gra}(G_n, S_i, E_{in})$, are considered to be the sum of the offset term $f_{Off}(G_n, E_{in})TF_{CMA}(E)$, which is independent of the variable S_i and the remaining term $f_{Rem}(G_n, S_i,$

E_{in})$TF_{CMA}(E)$. $TF_{CMA}(E)$ represents the CMA transmission function, and is written as TF_{CMA} below for brevity. Because the SE spectra of the substrate $J_{Sub}(S_i, E_{in})$ are the limiting cases of graphene spectra $J_{Gra}(G_n, S_i, E_{in})$, where any S_i-independent terms are zero, it follows that $J_{Sub}(S_i, E_{in}) = J_{Gra}(G_n = 0, S_i, E_{in}) = f_{Rem}(G_n = 0, S_i, E_{in})TF_{CMA}$. By separating the terms associated with the variable G_n, then $f_{Rem}(G_n, S_i, E_{in})TF_{CMA}$ could be rewritten as $f_{Tar}(G_n, S_i, E_{in})f_{Rem}(G_n = 0, S_i, E_{in})TF_{CMA}$ and then re-written as $f_{Tar}(G_n, S_i, E_{in})J_{Sub}(S_i, E_{in})$, where $f_{Tar}(G_n, S_i, E_{in})$ is equal to 1 when G_n is zero. Therefore, a measurement of graphene could be written as the following formula.

$$J_{Gra}\left(G_n, S_i, E_{in}\right) = f_{Off}\left(G_n, E_{in}\right)TF_{CMA} + f_{Tar}\left(G_n, S_i, E_{in}\right)J_{Sub}\left(S_i, E_{in}\right) \tag{3}$$

Substituting Eqn. 3 into Eqn. 2 gives:

$$\mathrm{D}_{\mathrm{Principle}}\left(\mathbf{b}, G_n, E_{in}\right) = \frac{b_1\left[f_{Tar}\left(G_n, S_B, E_{in}\right)J_{Sub}\left(S_B, E_{in}\right) - f_{Tar}\left(G_n, S_D, E_{in}\right)J_{Sub}\left(S_D, E_{in}\right)\right] + b_2\left[J_{Sub}\left(S_B, E_{in}\right) - J_{Sub}\left(S_D, E_{in}\right)\right]}{b_3\left[f_{Tar}\left(G_n, S_B, E_{in}\right)J_{Sub}\left(S_B, E_{in}\right) - f_{Tar}\left(G_n, S_D, E_{in}\right)J_{Sub}\left(S_D, E_{in}\right)\right] + b_4\left[J_{Sub}\left(S_B, E_{in}\right) - J_{Sub}\left(S_D, E_{in}\right)\right]}; \tag{4}$$

In Eqn. 4, only $f_{Tar}(G_n, S_i, E_{in})$ depends on G_n, which is the reason for naming it the "target" term. Because the principle descriptors should only be sensitive to G_n, the $J_{Sub}(S_i, E_{in})$ term, which only depends on E_{in} and is independent of G_n, must be cancelled in the numerator and denominator of Eqn. 4. To this end, $f_{Tar}(G_n, S_i, E_{in})$ is assumed to be independent of S_i as $f_{Tar}(G_n, E_{in})$, so Eqn. 4 can be rewritten as

$$\mathrm{D}_{\mathrm{Principle}}\left(\mathbf{b}, G_n, E_{in}\right) = \frac{b_1 f_{Tar}\left(G_n, E_{in}\right) + b_2}{b_3 f_{Tar}\left(G_n, E_{in}\right) + b_4}. \tag{5}$$

The assumption that $f_{Tar}(G_n, S_i, E_{in})$ is independent of S_i was verified by examining the consistency of $f_{Tar}(G_n, E_{in})$ when substituting different principle descriptors into Eqn. 5. Thus,

these principle descriptors only depend on $f_{\mathrm{Tar}}(G_{\mathrm{n}}, E_{\mathrm{in}})$. Considering that the selected principle descriptors are insensitive to E_{in}, $f_{\mathrm{Tar}}(G_{\mathrm{n}}, E_{\mathrm{in}})$ should also be insensitive to E_{in} and can therefore be further approximated as $f_{\mathrm{Tar}}(G_{\mathrm{n}})$. To confirm this, $f_{\mathrm{Tar}}(G_1)$ and $f_{\mathrm{Tar}}(G_2)$ at different E_{in} were calculated and found to be around 5% over the whole energy range as shown in Fig. 3, which is much smaller than the typical deviations between these SE spectra with different E_{in} of more than 30%.

Using $f_{\mathrm{Tar}}(G_{\mathrm{n}})$ instead of $f_{\mathrm{Tar}}(G_{\mathrm{n}}, S_{\mathrm{i}}, E_{\mathrm{in}})$, the expression of a measurement of graphene could be further updated to

$$J_{\mathrm{Gra}}\left(G_{\mathrm{n}}, S_{\mathrm{i}}, E_{\mathrm{in}}\right) = f_{\mathrm{Off}}\left(G_{\mathrm{n}}, E_{\mathrm{in}}\right) TF_{\mathrm{CMA}} + f_{\mathrm{Tar}}\left(G_{\mathrm{n}}\right) J_{\mathrm{Sub}}\left(S_{\mathrm{i}}, E_{\mathrm{in}}\right) \tag{6}$$

Based on Eqn. 6, the physical meaning of $f_{\mathrm{Tar}}(G_{\mathrm{n}})$ can be revealed with the help of a phenomenological picture of SE spectral measurement (the inset of Fig. 3). Physically, an SE spectrum of substrate-supported graphene includes contributions from two sources. The first source is the reflection from graphene, which typically contains SEs originating from the interaction of the high-energy monochromatic incident electrons with graphene when the electron beam is first incident on graphene. These SEs are reflected from graphene before interacting with the underlying Au substrate and are thereby functions of G_{n} and E_{in}, which match up with $f_{\mathrm{Off}}(G_{\mathrm{n}}, E_{\mathrm{in}})TF_{\mathrm{CMA}}$ in Eqn. 6. When the electron beam is incident on graphene, a transmission process also occurs. These transmitted electrons then interact with the underlying substrate and lead to a reflected spectrum. Furthermore, these substrate-reflected electrons subsequently pass through the graphene on the top of the substrate, forming the second source contributing to the obtained spectrum. Because of the complete transmission of high-energy electrons through the graphene film, the spectrum of the substrate-reflected electrons can be

reasonably approximated as that without graphene (i.e., $J_{Sub}(S_i, E_{in})$). In this case, the transmitted spectrum originating from these substrate-reflected electrons should be $J_{Sub}(S_i, E_{in})$ multiplied by the elastic electron transmission of graphene, which should depend on the single variable G_n, which has a value from 0 to 1, and perfectly match $f_{Tar}(G_n)$. Therefore, $f_{Tar}(G_n)$ is the elastic electron transmission of graphene and quantifies the possibility of energy loss by inelastic scattering when energetic electrons passed through the graphene layer.

It is worth mentioning that D_{23}, which has a **b** weight factor of [−1, 0, 0, −1], happens to have the same expression as $f_{Tar}(G_n)$. Here, D_{23} was produced completely digitally, but turned out to be a meaningful physical parameter, which in the past has only been obtained by carefully considering the physical picture throughout the whole process of data measurement [*21*]. In addition, $f_{Tar}(G_n)$, as quantitative graphene data, is obtained from the SE spectra, even though the TF_{CMA} of the instrumentation is unknown. That is, even though many instrumental parameters, such as pass energy, bias voltage, and magnetic shielding, could greatly affect SE spectral intensities, they will not affect the intensities of these selected principle descriptors. This is because the instrumental effects are counteracted via subtraction and ratioing between SE spectra measured with the same instrumental parameters.

3. Results

3.1. Extracting EAL and IMFP of graphene

The EAL of graphene (λ_{EAL}) was determined from $f_{Tar}(G_n)$ using the standard relationship of a straight-line approximation [*22*] by

$$\lambda_{EAL} = -\left(G_n d_0\right) / \left(\ln f_{Tar}\left(G_n\right) \cdot \cos\theta\right) \tag{7}$$

292 where d_0 is the thickness of a graphene layer (3.35 Å) and θ is the emission angle. Considering

293 that the expression of $D_{39}(G_n)$ is $\frac{1+f_{\mathrm{Tar}}(G_{\mathrm{n}})}{1-f_{\mathrm{Tar}}(G_{\mathrm{n}})}$ which could be further approximated to

294 $-\ln f_{\mathrm{Tar}}(G_{\mathrm{n}})/2$ Eqn. 7 could be updated to

295 $$\lambda_{\mathrm{EAL}} \approx (G_{\mathrm{n}} d_0)/(2D_{39}(G_{\mathrm{n}})\cdot\cos\theta) \quad (8)$$

296 In Eqn. 8, λ_{EAL} is the ratio of the electron flight length in graphene ($G_n d_0/\cos\theta$) to $D_{39}(G_n)$;

297 thereby, in a sense, $D_{39}(G_n)$ produced completely digitally is an undefined important physical

298 parameter related to λ_{EAL}. Furthermore, Eqn. 8 also provides a theoretical basis that supports that

299 λ_{EAL} is one of the best descriptors to summarize the essential information of a target sample from

300 electron beam-based measurements, even if its definition was created seemingly inadvertently

301 according to several modifications of the definition of attenuation length based on human

302 experience [*23*].

303 The resulting λ_{EAL} for both mono- and bilayer graphene are plotted in Fig. 4. At E above 150 eV,

304 the λ_{EAL} values determined for mono- and bilayer graphene are broadly consistent with each

305 other except around the C KVV Auger electron energy range, where the disagreement originates

306 from the different levels of overestimation of λ_{EAL} caused by the accompanying C KVV Auger

307 electrons in mono- and bilayer graphene. However, at E below 150 eV, marked differences

308 between λ_{EAL} of mono- and bilayer graphene are observed. The λ_{EAL} values of monolayer

309 graphene are about 20% lower than those of bilayer graphene in the energy range of 10–150 eV.

310 This deviation is probably the result of two factors. One is the difference between the electronic

311 states in monolayer graphene and bilayer graphene. The other is that the accompanying SE

312 contributions excited when the substrate-reflected electrons pass through the graphene layer,

313 which can no longer be neglected in the case of bilayer graphene. This point can be proved by
314 the comparison of the presented λ_{EAL} values with other independently measured or calculated
315 λ_{EAL} values. The λ_{EAL} values predicted by a newly developed hybrid method (see Appendix C) at
316 50 eV and 100 eV for both mono- and bilayer graphene show excellent agreement with the
317 presented λ_{EAL} values for monolayer graphene. Furthermore, the λ_{EAL} values measured with the
318 overlayer method using the AES technique for a graphene/nickel sample at 57 eV (Ni MVV
319 spectra) [*24*], for a graphene/silica (SiO_2) sample at 78 eV (Si LVV spectra) [*24*], and for a
320 graphene/buffer layer/SiC sample at 48 eV, 228 eV, 298 eV and 498 eV (Si 2p spectra) [*25*],
321 measured using synchrotron photoelectron spectroscopy, also agree well with the presented λ_{EAL}
322 values, particularly for monolayer graphene at E below 100 eV. We present the details in
323 Appendix D. Considering the excellent agreement between the presented λ_{EAL} values for both
324 mono- and bilayer graphene with those measured by AES at 503 eV (O KLL spectra) for a
325 graphene/SiO_2 sample, the present λ_{EAL} data for monolayer graphene should be recognized as
326 reliable, at least in the energy range of 50–600 eV.
327 Some principle descriptors can even be further exploited using conventional spectral analysis
328 approaches. Here, the reverse Monte Carlo (RMC) technique [*26*] was used to extract the IMFP
329 of monolayer graphene (λ_{IMFP}) from $D_{23}(G_n)$. The details can be found in Appendix E. The
330 resulting λ_{IMFP} values averaged for the three different incident energies are plotted in Fig. 5. For
331 comparison, we also included the λ_{IMFP} values for bulk graphite obtained experimentally by
332 EPES [*11*] and for both bulk graphite and graphene calculated theoretically by the extended
333 Mermin (EM) method [*27*]. As illustrated in Fig. 5, the presented λ_{IMFP} values of monolayer
334 graphene agreed well with the data calculated by the EM method except for at the C KVV Auger
335 electron energy. It is obvious that the λ_{IMFP} values of monolayer graphene are much higher than

336 those of bulk graphite. We also included the λ_{IMFP} values of a fictitious graphite surface in Fig. 5
337 in addition to those of bulk graphite, which is roughly estimated from the dielectric response of
338 an individual graphite surface by means of the surface energy loss function Im{−1/ε+1} [*28*],
339 where ε is the bulk dielectric function of graphite [*29*]. It is not surprising that the presented λ_{IMFP}
340 values of monolayer graphene are somewhere between those of bulk graphite and the fictitious
341 graphite surface. This implies that an inherent property of any nanomaterial is that their character
342 is strongly affected by the associated surface.

343 **3.2. Low-energy electron transmissivity**

344 The presented data-driven analysis was performed again for the energy range 0–50 eV, using the
345 corresponding SE spectra included in Appendix A to provide fine structure information. The
346 resulting $D_{23}(G_1)$, i.e., elastic electron transmission of monolayer graphene, are plotted in Fig. 6a.
347 They approximate transmission because the electrons are not significantly inelastically scattered
348 in the graphene layer at this low energy range.

349 In the transmission data, there were significant fluctuations in electron energy that were mainly
350 attributed to the diffraction of the crystal potential at certain energies. These fluctuations become
351 weaker with increasing electron energy because the electrons are elastically scattered to a lesser
352 extent by the potential change at higher energies. Over the whole energy range, three significant
353 high-transmission peaks at E = 0–10 eV, E = 14–22 eV, and E = 28–34 eV (highlighted by red
354 arrows) can be identified. In graphene, these peaks are often low-reflectivity valleys in low-
355 energy electron microscopy (LEEM) [*30,31*]. For comparison, the transmission of monolayer
356 graphene that was roughly estimated by LEEM of graphene on a SiC substrate [*30*] are plotted in
357 Fig. 6b. The two data sets are similar with respect to the electron energy, especially over 10–50
358 eV, where consistently high-transmission peaks can be observed. To further investigate these

359 peaks, an electronic band structure of graphene in the Γ−A direction was calculated via the
360 "graphene pseudo-crystal" [*32*] first-principles method. The details of first-principles
361 calculations are presented in Appendix G. The graphene interlayer distance was set to 6 Å, rather
362 than the 3.35-Å interlayer distance in graphite, and plotted in Fig. 6c. The peaks observed in both
363 the presented transmission data and from LEEM perfectly correspond to dispersive bands at the
364 same energies over the whole range, except for the 0–5 eV range. At the low energies, deviations
365 between transmission data and the bulk graphite band structure derive from graphene-substrate
366 interactions. Nevertheless, the results reveal that electrons at appropriate energies can couple to
367 the allowed states and have larger transmission probabilities through graphene.
368 To investigate the contribution of graphene-Au interactions in the presented transmission data,
369 the intensities were compared with those from a suspended graphene sample. For 0–5 eV, the
370 intensities of the presented transmission data are 80–90%, with relatively large error bars
371 because of small SE intensities. Above 5 eV, the transmission intensities decreased sharply up to
372 10 eV, and then stabilized at 50–60% in the 10–50 eV range. It should be noted that the high
373 transparency of monolayer graphene over the range 0–5 eV is in contrast to previous results that
374 were lower than 2% at *E* below 5 eV [*33*]. However, Srisonphan et al. [*34*] reported 99.9%
375 transparency below 3 eV for monolayer graphene suspended on a trenched metal-oxide-
376 semiconductor diode. Kojima et al. [*35*] also suggested high transmissivity of quasi-ballistic
377 electrons from a nanocrystalline porous Si cold cathode and a monolayer graphene surface
378 electrode. Scatter in the data at 2.3 eV is due to the plasmon gain phenomenon in the Au
379 substrate [*36*]. The electron transmissivity of graphene exhibits a maximum at 5 eV, which is
380 consistent with that of Mikmekova et al. [*37*] for a suspended monolayer sample using LEEM in
381 a scanning transmission electron microscope. The 50–60% intensities over the range 10–50 eV

agree well with previous results [*38*] from a suspended graphene sample. In that case, the graphene transparency was 60% over 10–40 eV using vacuum-three-electrode configurations. According to the above discussion, graphene-Au interactions were significant at E below 10 eV, but negligible over the 10–50 eV range. Therefore, quantitative information on suspended graphene can be approximated with an Au-supported graphene sample with acceptable accuracy at E above 10 eV, even though the electronic properties of graphene are affected by the underlying Au substrate. For example, the π-orbitals of the sp^2-hybridized graphene atoms are coupled to the *d*-orbitals of the Au atoms [*39*], and the graphene surface is reconstructed on an Au(111) substrate [*40*].

3.3. Low-energy EAL and IMFP determination

The λ_{EAL} values of monolayer graphene obtained from the $D_{23}(G_1)$ in the energy range of 0–50 eV are plotted in Fig. 7 together with those of single-crystal graphite obtained by very-low-energy electron diffraction [*41*]. In the energy range of 0–6 eV, λ_{EAL} of monolayer graphene shows an obvious peak structure at 4-5 eV similar to that of single-crystal graphite. Such peak structure in the λ_{EAL} values of graphene perfectly explains the features of the SE main peak observed in the spectra measured for substrate-supported graphene, because the substrate-reflected SEs are modulated by this peak structure when they pass through the covering graphene layer. In the energy range around 2.3 eV, λ_{EAL} values of monolayer graphene are scattered because of the influence from surface plasmons of the underlying Au substrate. In this region, one independent λ_{EAL} value of graphene at ~2.3 eV can be measured by the overlayer method according to the attenuation of surface plasmons of Au (approximately equalling the attenuation of electrons) by graphene sheets [*36*]. This independent λ_{EAL} data point is also plotted in Fig. 7

and is broadly consistent with the λ_{EAL} values determined by the data-driven spectral analysis method, which improves the credibility of the presented λ_{EAL} data.

As for E above 6 eV, although similar fluctuations of E in the λ_{EAL} data were observed for both monolayer graphene and single-crystal graphite, the intensity of the fluctuations in λ_{EAL} of monolayer graphene was much weaker than that of single-crystal graphite, which is because of the vastly suppressed diffraction effect in monolayer graphene compared with that in single-crystal graphite.

For comparison, the λ_{EAL} energy-filtered SEM data for a graphene/nickel sample [*42*] is also plotted in Fig. 7. These data have larger values than the presented λ_{EAL} data in the overlapping energy range, especially for E lower than 18 eV. There are two reasons for the deviations. One reason is that the interactions between graphene and an Au substrate are relatively weak compared with those between graphene and Ni. The other reason is the oversimplified overlayer method used in Ref. [*42*] to determine the λ_{EAL} data, where the elastic electron transmission of graphene is roughly approximated by the ratio of SE signals measured on graphene to that measured on substrate, i.e. $J_{Gra}(G_n, S_i)/J_{Sub}(S_i)$. According to Eq. 6, $J_{Gra}(G_n, S_i)/J_{Sub}(S_i)$ can be rewritten as the sum of $f_{Tar}(G_n)$ and $f_{Off}(G_n, E_{in})TF_{CMA}/J_{Sub}(S_i)$. Although $f_{Tar}(G_n)$ is the elastic electron transmission of graphene, $f_{Off}(G_n, E_{in})TF_{CMA}/J_{Sub}(S_i)$ originating from those SEs excited and emitted from graphene when electron beam is first incident is the error source in calculating the λ_{EAL} data. This could result in an overestimation of the λ_{EAL} data, especially at very low E (18 eV), where the intensity of SEs excited and emitted from graphene sharply increase.

The λ_{IMFP} values of monolayer graphene were also determined from these more detailed SE spectra with the help of RMC calculations at E above 6 eV. The presented λ_{IMFP} values of graphene were higher than the λ_{EAL} values of graphene because of the removal of the elastic

427 scattering effect from λ_{IMFP}. However, it is unusual that the λ_{EAL} data showed weak dependence
428 on E whereas the λ_{IMFP} data showed strong fluctuations of E at certain energies. In the case of a
429 bulk material, inelastic scattering generally results in a simple dependence of λ_{IMFP} on energy as
430 a well-known universal curve [*43*] and the elastic scattering results in diffraction minima in the
431 λ_{EAL} curve. The fluctuations of E in the λ_{IMFP} data probably originated from the coupling between
432 the crystal potential of monolayer graphene and that of the surface layer of the underlying Au
433 substrate, which remained in the presented λ_{IMFP} data because of the oversimplified RMC
434 program. This conjecture is supported by the observed λ_{EAL} data, because similar fluctuations of
435 E were observed in the λ_{EAL} values determined for both monolayer graphene and single-crystal
436 graphite. The λ_{EAL} and λ_{IMFP} of monolayer graphene determined from the presented transmission
437 data correspond to Au-supported graphene over the whole energy range. However, as discussed
438 above, they can be used to approximate those of suspended graphene at E above 10 eV.
439 Last but not least, it is not surprising that the λ_{EAL} values of monolayer graphene were much
440 higher than those of single-crystal graphite at E below 50 eV, which is in accordance with the
441 observations of λ_{IMFP} in the energy range of 50–600 eV, as shown in Fig. 5. These results
442 indicate that the possibility of an electron colliding with monolayer graphene is very low
443 compared with that of an electron colliding with graphite, resulting in monolayer graphene
444 possessing an ultralow SE yield, which is consistent with a recent experimental observation [*44*]
445 and recent theoretical calculations [*45*].

446 **4. Discussion**

447 Using AD descriptors to separate useful information from collected SE signals has a long
448 history, however, a paradigm for designing useful AD descriptors has not yet emerged. The
449 widely used spectral subtraction and spectral ratioing techniques are the simplest approaches that

employ AD descriptors, which entail the subtraction or ratioing, respectively, of two interrelated measurements to highlight interesting spectral features. When these two simple techniques are insufficient to extract useful information from SE signals, more complex AD descriptors are developed via subtraction and ratioing between two interrelated measurements to enlarge small differences between the two measurements, such as D_{28} in Ref. [*19*] and D_{33} in Ref. [*20*]. When these AD descriptors fail, the complexity can be increased with more than two interrelated measurements. For example, the four-point probe technique in materials science precisely determines electrical resistance by excluding contributions from parasitic contact resistances [*46*], the chop-nod method in radio astronomy detects faint astronomical sources against the bright, variable sky background using ground-based telescopes [*47*], and the virtual substrate method in surface analysis characterizes nanomaterials without effects from the underlying substrate [*21*]. These are examples of three well-designed AD descriptors constructed from more than two interrelated measurements. This paper attempts to provide a paradigm for the construction of well-designed AD descriptors according to the given requirements. The presented data-driven spectral analysis method is an extension of conventional spectral analyses with the goal of comprehensive exploration of AD descriptors. By using this extension, we improve our chance of finding well-designed AD descriptors that meet realistic requirements according to the experience garnered from many measurements under different experimental conditions, which is particularly important for reaching a quantitative understanding of backgrounds.

5. Conclusion

In summary, we developed a data-driven spectral analysis method to measure the electron transport properties of monolayer graphene, which is particularly incisive in the low-energy regime. Instead of focusing on the spectral features observed in an individual spectrum, we used

AD descriptors to extract quantitative information about graphene hidden in the interrelationship of absolute intensities of the SE spectra measured under slightly different conditions. This new method measured both λ_{EAL} and λ_{IMFP} of monolayer graphene over the whole energy range in parallel using one set of SE spectra. In addition, this technique extended the analysable energy scale to the levels of only several electron volts, which allowed the continuous extraction of electron–electron interactions in graphene down to a very low energy scale. This method also holds potential to extract much other useful information hidden in SE backgrounds beyond that of electron–electron interactions when different selection criteria for AD descriptors or different experimental variables are used. The developed method can be readily extended to other 2D materials such as 2D magnets and may provide useful information about electron exchange interactions and dimensional-dependent magnetism. Furthermore, the application of this method could even extend beyond materials science to many other fields where electron interactions play important roles, such as 2D material-based quantum information technology.

Acknowledgements We thank Dr. C. J. Powell, Prof. Tarakura, and Prof. Tanaka for helpful comments and discussions. We thank Prof. M. S. Xu for providing the AES data for graphene on a Ni substrate and graphene on a SiO2 substrate. We thank Prof. Homma for providing the EAL data of monolayer graphene measured using energy-filtered SEM. We thank Dr. Y. Ueda and Prof. K. Watanabe for performing the TDDFT calculation. This work was supported by the "Materials Research by Information Integration" Initiative (MI2I) Project of the Support Program for Starting Up Innovation Hub from the Japan Science and Technology Agency (JST). K.T. was supported by a Grant-in-Aid (grant no. 18K18868) from Ministry of Education, Culture, Sports, Science and Technology (MEXT). J.H. was supported by the U.S. Department of Energy (DOE), Office of Science, Office of Basic Energy Sciences under Award DE-SC0019467. Z.J.D was supported by the National Natural Science Foundation of China (No. 11574289). All DFT calculations were performed on the Numerical Materials Simulator supercomputer at the National Institute for Materials Science (NIMS).

Appendix A: SE spectra of graphene/Au sample

1. Substrate preparation

Au layers (200 nm) were evaporated at rates of 0.2 nm s^{-1} on Si(100) substrates with Ti buffer layers (5 nm) pre-evaporated at rates of 0.05 nm s^{-1} by electron-beam evaporation (RDEB-1206K, R-DEC Co. Ltd., Ibaraki, Japan) with a chamber pressure of ~1.0×10^{-5} Pa. After evaporation, the samples were annealed by rapid thermal annealing (QHC-P410, Ulvac-Riko Inc., Kanagawa, Japan) under an N_2 atmosphere at 300 °C for 30 s. The relative orientation between bright and dark regions on the polycrystalline Au substrate measured by electron backscatter diffraction was about 4°. The SEM, and electron backscatter diffraction (EBSD) images of the polycrystalline Au substrate are presented in Fig. 8.

2. Graphene fabrication

Graphene flakes were produced on the Au substrates by mechanical exfoliation. These graphene layers on the Au substrates can be considered as quasi-free-standing graphene layers that have ignorable lattice mismatch and similar electronic properties to those of free-standing graphene layers. The number of graphene layers was confirmed by Raman spectroscopy. The SEM images of graphene/Au samples are presented in Fig. 8.

3. SE spectra measurement.

SE spectra were measured at room temperature with a scanning Auger electron spectrometer (SAM650, Ulvac-Phi, Kanagawa, Japan) with a CMA (Fig. 1a). The take-off angle of the instrument was 42.3±6°. The incident electron beam current for the raw spectra was ~0.87 nA, as calibrated with a Faraday cup before the measurements. To minimize the influence of changes in the stability of the instrument over time, short-term repeated measurements for multiple cycles at different measurement sites were used. Two groups of SE spectra were measured independently

from the same sample at similar measurement sites in the energy ranges of 0–50 and 0–600 eV, as shown in Fig. 9 and 10, respectively. Each group contained 18 different types of SE spectra measured at bright and dark regions on the bare substrate and similar neighbouring regions covered by monolayer graphene or bilayer graphene sheets with E_{10}, E_{15}, and E_{20}. Each SE spectrum was averaged from eight different sample regions on the bare substrate as well as on mono- or bilayer graphene samples.

Appendix B: AD descriptors

1. Sensitivities of AD descriptors

Like the measured SE spectra, the AD descriptor D(**a**, G_n, E_{in}) is also a function of E but E has been omitted from the expression for simplicity. Furthermore, the expansion of D(**a**, G_n, E_{in}) in terms of E is [d_1, d_2, …, d_M] (omitting the variables), where d_j is the calculated value at a given E and M is the number of points in the energy axis of spectra.

Score1, which quantifies the sensitivity of the descriptor to E_{in}, was calculated for every candidate descriptor using the following formula:

$$\mathrm{Score1}\left[\mathrm{D}(\mathbf{a})\right] = \frac{1}{NM}\sum_{n=1}^{N}\sum_{j=1}^{M} c_v\left[\mathrm{d}_j\left(\mathbf{a}, G_\mathrm{n}, E_\mathrm{in}\right)\right], \tag{B1}$$

where Score1[D(**a**)] is the sensitivity of a descriptor determined by a given weight factor **a** to E_{in} and d_j(**a**, G_n, E_{in}) is the component of the AD descriptor D(**a**, G_n, E_{in}) at a given E_j. The coefficient of variation ($c_v = \sigma/\mu$) of the component of descriptor d_j(**a**, G_n, E_{in},) with respect to E_{in} was used to estimate the sensitivity and further averaged over M (M = 600) data points in the measured SE spectra and over the number of different graphene layer numbers N (N = 2).

Score2 was used to quantify the sensitivity of a descriptor to G_n as:

$$\text{Score2}\left[\mathrm{D}(\mathbf{a})\right] = \frac{1}{LM}\sum_{k=1}^{L}\sum_{j=1}^{M}\sqrt{\tilde{\chi}^2\left(\mathrm{d}_j\left(\mathbf{a}, G_\mathrm{n}, E_\mathrm{in}\right)\right)}, \tag{B2}$$

where Score2[D(**a**)] is the sensitivity of a descriptor determined by a given weight factor **a** to G_n. Here, a variant of the square root of the χ^2 formula ($\tilde{\chi}^2 = \sum_i \frac{(\mathrm{O_i} - \mathrm{E_i})^2}{\mathrm{E}_i^{\,2}}$) was used to estimate the sensitivity where the observed frequencies $\mathrm{O_i}$ and expected frequencies $\mathrm{E_i}$ were replaced by the component value of descriptor $\mathrm{d}_j(\mathbf{a}, G_\mathrm{n}, E_\mathrm{in})$ and the mean value of these $\mathrm{d}_j(\mathbf{a}, G_\mathrm{n}, E_\mathrm{in})$ were averaged for different G_n. Furthermore, these calculated sensitivities were averaged from M (M = 600) data points in the measured spectra and L (L = 3) options of E_in. The Pareto optimal descriptors sorted out from the candidates according to their Score1 and Score2 are listed in Table 1.

2. Coefficient of variation of principle descriptors

The coefficient of variation ($c_v = \frac{\sigma}{\mu} = \frac{\sqrt{\sigma_{1\mathrm{L}}^2 + \sigma_{2\mathrm{L}}^2}}{\mu_{1\mathrm{L}} - \mu_{2\mathrm{L}}}$) was used to evaluate whether or not the deviations of the Pareto optimal descriptors caused by different G_n was sufficiently large to be observed under disturbance of the deviations caused by different E_in, where $\mu_{1\mathrm{L}}$, $\sigma_{1\mathrm{L}}$, $\mu_{2\mathrm{L}}$, and $\sigma_{2\mathrm{L}}$ are mean values ($\mu_{1\mathrm{L}}$, $\mu_{2\mathrm{L}}$) and standard deviations ($\sigma_{1\mathrm{L}}$, $\sigma_{2\mathrm{L}}$) of the summed descriptor ($\sum_{j=1}^{M}\mathrm{d}_j\left(\mathbf{a}, G_\mathrm{n}, E_\mathrm{in}\right)$) for mono- ($\mu_{1\mathrm{L}}$, $\sigma_{1\mathrm{L}}$) and bilayer ($\mu_{2\mathrm{L}}$, $\sigma_{2\mathrm{L}}$) graphene with respect to E_in. Nine principle descriptors sorted out from the Pareto optimal descriptors according to its coefficient of variation are presented in Fig. 11 and their weight factors **a** are listed in Table 2.

Appendix C: Hybrid method to predict λ_{EAL}

The λ_{EAL} values for free-standing mono- and bilayer graphene samples were roughly estimated at 50 and 100 eV by a hybrid method using a combination of the time-dependent density functional

565 theory (TDDFT) method [48] and MC method [49]. In this calculation, transmitted electrons
566 with both the inelastic and elastic components were modelled using a TDDFT simulation in real
567 time and space by representing the incident electrons as finite-sized wave packets [50].
568 Subsequently, to determine λ_{EAL}, the elastic component was derived with the help of the MC
569 method, from which the proportion of elastic electrons was estimated. The MC simulation of
570 electron trajectories penetrating a sample was based on a description of individual electron
571 scattering processes; i.e., elastic scattering and inelastic scattering. The elastic scattering cross-
572 section of a carbon atom [51] used herein was that described by the muffin-tin potential
573 approximation. Furthermore, the inelastic scattering cross-section was determined by the EM
574 method [*27*] from the energy loss function of graphene calculated using the WIEN2k package
575 [52].

576 **Appendix D: Overlayer method.**

577 The λ_{EAL} values were measured by the overlayer method. The Ni MVV, Si LVV, and O KLL
578 spectra collected from the bare substrate and covering graphene layer are presented in Fig. 12a,
579 b, and c, respectively, from which the contributions from Auger electrons were extracted using
580 the Tougaard background removal technique [53]. The standard relationship between λ_{EAL} and
581 the attenuated Auger signal in G_n layers of graphene is given by

582 $$\lambda_{\mathrm{EAL}} = \frac{G_{\mathrm{n}} d_0}{\ln\left(I_0/I_{\mathrm{n}}\right)\cdot\cos\theta} \quad \text{(D1)}$$

583 where d_0 is the thickness of a single graphene layer (3.35 Å); I_{n} and I_0 are the Auger signal
584 intensities attenuated by G_n layers of graphene and that from a bare substrate (G_n = 0),
585 respectively; and θ is the emission angle with respect to the sample normal. According to Eqn.
586 D1, λ_{EAL} can be obtained at 57, 78, and 503 eV, which correspond to the Ni MVV, Si LVV, and

587 O KLL transitions, respectively. Log plots of the Auger signal intensity attenuation of these
588 spectra as a function of G_n are presented in Fig. 12d, e, and f together with their fitting lines.
589 From these plots, it is easy to estimate λ_{EAL} at 57, 78, and 503 eV corresponding to the Ni MVV,
590 Si LVV, and O KLL transitions, respectively. The averaged λ_{EAL} values estimated from the AES
591 measurements collected for different G_n are 4.6, 6.0, and 22.0 Å for the transitions at 57, 78, and
592 503 eV, respectively.

593 **Appendix E: RMC method to predict λ_{IMFP}**

594 The λ_{IMFP} of monolayer graphene was extracted from $D_{23}(G_1)$ by the RMC technique [*26*]. The
595 RMC program used herein can be summarized as an iterative process to improve λ_{IMFP} in a
596 conventional MC simulation of electron interaction with monolayer graphene. This improvement
597 was accomplished by minimizing the differences between the simulated and measured elastic
598 electron transmission of monolayer graphene. In this program, we used a fixed elastic scattering
599 cross-section of a carbon atom described by the muffin-tin model potential [52] to approximate
600 the elastic scattering effects in monolayer graphene along the out-of-plane direction. It should be
601 noted that this RMC program is valid only for monolayer nanomaterials, where it is appropriate
602 to neglect the diffraction effect in the out-of-plane direction [54]. A flow chart of this RMC
603 program is provided in Fig. 13a, wherein the MCMC sampling process is omitted for clarity. The
604 algorithm is as follows:

605 (1) The initial λ_{IMFP} values can be chosen as arbitrary positive numbers, but this would result in a
606 much longer convergence time. We started with λ_{IMFP} calculated based on the extended
607 Mermin (EM) method from the energy loss function determined by a WIEN2k program
608 package.

(2) Based on these λ_{IMFP} values, an MC simulation was performed to obtain the elastic transmission spectrum, $I_0^{\mathrm{sim}}\left(E_j\right)$, where the index j denotes the jth experimental grid value of the electron energy E. The simulation procedure was the same as that previously used to calculate the elastic transmission of graphene (Fig. 13b).

(3) The sum of least-squares relative differences between the experimentally measured elastic transmission spectrum, $I^{\mathrm{exp}}(E_j)$, and MC-simulated spectrum, $I_0^{\mathrm{sim}}\left(E_j\right)$, was calculated

$$\chi_0^2 = \sum_j \left\{ \left[I_0^{\mathrm{sim}}\left(E_j\right) - I^{\mathrm{exp}}\left(E_j\right) \right] \Big/ \sigma\left(E_j\right) \right\}^2, \tag{E1}$$

where the summation is taken over E_j. The parameter $\sigma(E_j)$ is an artificially specified weighting factor spectrum whose effect is to accelerate the convergence process. The parameter $\sigma(E_j)$ can be considered as "temperature" in the simulated annealing and can be set as a constant in this RMC program because of the sufficient accuracy achieved by an initial "temperature" set. This removes the need for a gradual "temperature" decrease such as that used in the conventional simulated annealing method. Each χ^2 value defines the "potential energy" to be minimized in an MCMC simulation.

(4) The graphene λ_{IMFP} values were adjusted at random in a specified range, although the randomness was directed using the known negative correlation between λ_{IMFP} and simulated elastic transmission. Specifically, a larger λ_{IMFP} leads to a smaller transmission, whereas a smaller λ_{IMFP} leads to a larger transmission. New inelastic scattering cross sections were then obtained with the help of the energy loss probability determined by the EM method (Fig. 13c). Based on this new inelastic scattering cross section combined with the unaltered elastic scattering cross section, a new MC simulation was performed with the help of the EM-

determined energy loss probability of graphene to derive an updated spectrum, $I_1^{\mathrm{sim}}\left(E_j\right)$. This step produced a new "potential energy":

$$\chi_1^2 = \sum_j \left\{ \left[I_1^{\mathrm{sim}}\left(E_j\right) - I^{\mathrm{exp}}\left(E_j\right) \right] \Big/ \sigma\left(E_j\right) \right\}^2. \tag{E2}$$

(5) The change of the potential energy in this MCMC step was calculated as $\Delta\chi_1^2 = \chi_1^2 - \chi_0^2$. If $\Delta\chi_1^2 > 0$, then the move was accepted only with the probability $\exp\left(-\chi_1^2\right) \big/ \exp\left(-\chi_0^2\right) = \exp\left\{-\left(\chi_1^2 - \chi_0^2\right)\right\}$ according to Metropolis importance sampling, where the "temperature" factor in a Boltzmann distribution has already been included in $\sigma(E_j)$ as its absolute values. Otherwise, the move was rejected, and we repeated step 4 by adjusting the λ_{IMFP} with other values. It should be noted that because the λ_{IMFP} values are independent of energy, the MCMC sampling procedure for optimizing the λ_{IMFP} values at different energies was performed in parallel.

(6) Step 4 and 5 were repeated for the next iteration. Successive iterations generated decreasing values of potential energy χ_i^2 until they reached a minimum value. These minimum values possessed only a slight fluctuation where the difference between the simulated elastic transmission spectrum and measured spectrum was negligible.

In this way, our RMC simulation procedure can automatically optimize the λ_{IMFP} of graphene to obtain the smallest difference between the simulated and measured elastic transmission data. It is particularly important that this RMC method uses the MCMC principle to accelerate the global optimization of the parameter set, which guarantees that the final results are independent of the initial λ_{IMFP} values. Fig. 13d shows the progression as the λ_{IMFP} values are updated, as well as the simulated elastic transmission spectra resulting from the RMC process. The change in the

651 normalized least-squares values χ_i^2/χ_0^2 with each MCMC step is also given in Fig. 13e. The
652 calculation time necessary to obtain satisfactory convergence (100 successive MCMC steps) was
653 about 1 h with one CPU (Intel Core i7-3520M running at 2.90 GHz). It is obvious that the final
654 simulated elastic transmission spectrum (100 successive steps) fits the experimental spectrum
655 very well. This is true even though the noise in the measured elastic transmission was completely
656 transferred to the determined graphene λ_{IMFP}, which was then enhanced in the high-energy range.
657 This enhancement is caused by the dominant role that λ_{IMFP} plays in determining the electron
658 transport behaviour at high energies. It was found that the fine structures observed in the
659 determined λ_{IMFP} corresponded precisely to the structures in the measured elastic transmission
660 spectrum. This implies that the accuracy of the determined λ_{IMFP} is mainly regulated by the
661 accuracy of the measured elastic transmission. It should be noted that the Mott cross sections
662 based on the muffin-tin potential model for describing elastic scattering are well-trusted for
663 electron energies (E) above 50 eV (with reference to the vacuum level), but may be questionable
664 below this energy. Because the Fermi level of monolayer graphene is at 25.4 eV, the limit for
665 trustworthiness will shift to energies below 25.4 eV, where the constant electronic potential
666 ($E_{\mathrm{F}}+\varphi$) in monolayer graphene is 24.6 eV. To assess the reliability of the determined λ_{IMFP} values
667 of graphene below this limit, tests were performed wherein elastic cross sections based on
668 different atomic potential models were used in the RMC program for the same experimental
669 elastic transmission data measured with an incident electron energy of 10 keV. The resulting
670 λ_{IMFP} values and corresponding simulated elastic transmission spectra after 50 successive MCMC
671 steps are shown in Fig. 13f and g for the E ranges of 0–600 and 0–50 eV, respectively. The final
672 IMFP values and simulated elastic transmission converged above 25 eV even with different
673 elastic scattering cross sections. This implies that at E greater than 25 eV, the electron transport

behaviour inside monolayer graphene is mainly determined by inelastic scattering. The excellent agreement between various atomic potential models for E above 25 eV also provides clear evidence for the reliability of the determined λ_{IMFP} in this range. However, elastic scattering plays an increasingly important role in the elastic transmission spectrum when E is below 25 eV, which is evidenced by the observed deviations of the determined λ_{IMFP} values between different atomic potential models even though they still predicted the same elastic transmission spectrum. Therefore, the accuracy of the determined λ_{IMFP} can only be determined by the accuracy of the elastic scattering cross section, including the selection of atomic potential model. Although there is no direct evidence for its accuracy below 50 eV (25.4 eV refers to the Fermi level), the muffin-tin potential model is one of the best and most popular atomic potentials even at such low E. Therefore, the presented λ_{IMFP} values of monolayer graphene in the E range of 10–25 eV are considered to be relatively reliable. This corresponds with the reliability of the elastic scattering cross sections determined based on the muffin-tin model potential in the E range of 35–50 eV (10–25 eV relative to the Fermi level). When E was 6 eV, even the simulated elastic transmissions based on the muffin-tin model potential did not agree with the measured transmissions regardless of any reasonable adjustments of the tentative λ_{IMFP}. The reasonableness of the λ_{IMFP} value was judged by whether or not a reasonable SE spectrum was obtained by the MC method using this λ_{IMFP} value. This result implies that either the calculated elastic scattering cross section or measured elastic transmission at very low E is inaccurate.

Appendix F: Empirical formulas for λ_{IMFP}

The Bethe equation [55] was used to analyse the energy dependence of the presented λ_{IMFP} of monolayer graphene at E above 50 eV except for the C KVV Auger electron energy range. The Bethe equation is written as

$$\lambda_{\mathrm{IMFP}} = E \Big/ \left[E_p^2 \beta \ln\left(\gamma E\right) \right], \tag{F1}$$

where E_p is the free-electron plasmon energy (in eV) (for carbon E_p = 22.3 eV), and β and γ are material-dependent parameters (β = 0.0098 $\mathrm{eV}^{-1}\cdot\mathrm{Å}^{-1}$ and γ = 0.053 eV^{-1}). The fitted curve is plotted in Fig. 5 as a visual guide.

Appendix G: Electronic structure of graphene

First-principles, total-energy calculations were performed within the framework of density-functional theory [56,57], as implemented in the Quantum Espresso code [58]. Projector augmented wave pseudopotentials were used to describe the electron-ion interaction [59]. The valence wave functions and augmented charge density were expanded using a plane-wave basis set with cutoff energies of 60 and 540 Ry, respectively. The electronic structure of a graphite crystal with experimental lattice parameters, and a "pseudo-graphene crystal" with an interlayer distance of 6 Å, were used to calculate the energy band. For a graphene-Au substrate, we used a slab model in which the Au thin film was simulated as a seven-layer Au(111) surface. The Au(111) thin film with $\sqrt{3}\times\sqrt{3}$ lateral periodicity was coated with a graphene monolayer with 2×2 lateral periodicity, in which the lateral lattice parameters of graphene were fixed to the optimized 2.928-Å lattice parameter of the Au(111) surface. A van der Waals-corrected density functional [60] for the exchange-correlation energy was used to accurately describe the weak binding between the Au(111) surface and the graphene. All atoms were fully optimized until the remaining force acting on each atom was less than 0.0001 Ry/Bohr. The Brillouin-zone integration was sampled by the Monkhorst-Pack (MP) scheme [61] with 42×42×1 k-point grids in the self-consistent field calculations for optimization structures and energy band structures. The corresponding results are presented in Fig. 14.

719

720 **References**

721 [1] C. S. Fadley and D. A. Shirley, X-Ray Photoelectron Spectroscopic Study of Iron, Cobalt,
722 Nickel, Copper, and Platinum. *Phys. Rev. Lett.* **21**, 980 (1968).

723 [2] G. L. Connell, Auger Electron Spectroscopy of Graphite Fibre Surfaces. *Nature* **230**, 377
724 (1971).

725 [3] C. R. Helms and W. E. Spicer, Verification of the Metal-Rich Surface Model for the
726 Oxidation of Sr, by Auger-Electron Spectroscopy. *Phys. Rev. Lett.* **32**, 228 (1974).

727 [4] J. J. McCarroll, R. W. Mould, H. B. Silver, and M. L. Sims, Auger electron spectroscopy of
728 wear surfaces. *Nature* **266**, 518 (1977).

729 [5] R. Addou, A. Dahal, and M. Batzill, Growth of a two-dimensional dielectric monolayer on
730 quasi-freestanding graphene. *Nat. Nanotech.* **8**, 41 (2013).

731 [6] C. H. Zhang, C. H. Jin, A. L. Koh, Y. Zhou, W. G. Xu, Q. C. Li, Q. H. Xiong, H. L. Peng,
732 and Z. F. Liu, Direct growth of large-area graphene and boron nitride heterostructures by a
733 co-segregation method. *Nat. Commun.* 6, **6519** (2015).

734 [7] R. C. Masters, A. J. Pearson, T. S. Glen, F.-C. Sasam, L. Li, M. Dapor, A. M. Donald, D. G.
735 Lidzey, C. Rodenburg, Sub-nanometre resolution imaging of polymer-fullerene photovoltaic
736 blends using energy-filtered scanning electron microscopy. *Nat. Commun.* **6**, 6928 (2015)

737 [8] ISO18115 *Surface* Chemical *Analysis—Vocabulary—Part 1: General terms and terms used*
738 *in spectroscopy* (International Organisation for Standardisation, Geneva, 2010).

739 [9] C. J. Powell, A. Jablonski, Evaluation of calculated and measured electron inelastic mean
740 free paths near solid surfaces. *J. Phys. Chem. Ref. Data* **28**, 19 (1999).

[10] G. Gergely, Elastic backscattering of electrons: Determination of physical parameters of electron transport processes by elastic peak electron spectroscopy. *Prog. Surf. Sci*. **71**, 31-88 (2002).

[11] S. Tanuma, T. Shiratori, T. Kimura, K. Goto, S. Ichimura, C. J. Powell, Experimental determination of electron inelastic mean free paths in 13 elemental solids in the 50 to 5000 eV energy range by elastic-peak electron spectroscopy. *Surf. Interface Anal*. **37**, 833-845 (2005).

[12] J. D. Bourke, C. T. Chantler, Measurements of electron inelastic mean free paths in materials. *Phys. Rev. Lett*. **104**, 206601 (2010).

[13] R. Zdyb, T. O. Menteş, A. Locatelli, M. A. Niño, E. Bauer, Inelastic mean free path from reflectivity of slow electrons. *Phys. Rev. B* **87**, 075436 (2013).

[14] I. Olefjord, H. J. Mathieu, P. Marcus, Intercomparison of surface analysis of thin aluminium oxide films. *Surf. Interface Anal*. **15**, 681-692 (1990).

[15] C. J. Powell, A. Jablonski, Electron effective attenuation lengths for applications in Auger electron spectroscopy and X-ray photoelectron spectroscopy. *Surf. Interface Anal*. **33**, 211-229 (2002).

[16] F. L. Battye, Photoelectron determination of the attenuation of low-energy electrons in Al_2O_3. *Phys. Rev. B* **9**, 2887 (1974).

[17] M. S. Xu, D. Fujita, J. H. Gao, N. Hanagata, Auger electron spectroscopy: A rational method for determining thickness of graphene films. *ACS Nano* **4**, 2937-2945 (2010).

[18] V. K. Mathur, How well do we know Pareto optimality? *J. Econ. Edu.* **22**, 172-178 (1991).

[19] H. Hiura, H. Miyazaki, K. Tsukagoshi, Determination of the Number of Graphene Layers: Discrete Distribution of the Secondary Electron Intensity Stemming from Individual Graphene Layers, *Appl. Phys. Express*, **3**, 095101 (2010).

764 [20] S. Giménez; A. L. Rogach, A. A. Lutich, D. Gross, A. Poeschl, A. S. Susha, I. Mora-Seró,
765 T. Lana-Villarreal, J. Bisquert, Energy Transfer versus Charge Separation in Hybrid Systems of
766 Semiconductor Quantum Dots and Ru-Dyes as Potential Co-Sensitizers of TiO2-Based Solar
767 Cells, *J. Appl. Phys.*, **110**, 014314 (2011).
768 [21] B. Da, J. W. Liu, M. Yamamoto, Y. Ueda, K. Watanabe, N. T. Cuong, S. L. Li, K.
769 Tsukagoshi, H. Yoshikawa, H. Iwai, S. Tanuma, H. X. Guo, Z. S. Gao, X. Sun, Z. J. Ding,
770 Virtual substrate method for nanomaterials characterization, *Nat. Commun*. **8**, 15629 (2017).
771 [22] P. J. Cumpson, M. P. Seah, Elastic scattering corrections in AES and XPS. II. Estimating
772 attenuation lengths and conditions required for their valid use in overlayer/substrate experiments,
773 *Surf. Interface Anal*. **25**, 430-446 (1997).
774 [23] A. Jablonski, C. J. Powell, The electron attenuation length revisited. *Surf. Sci. Rep.* **47**, 33-
775 91 (2002).
776 [24] M. S. Xu, D. Fujita, J. Gao, and N. Hanagata, Auger Electron Spectroscopy: A Rational
777 Method for Determining Thickness of Graphene Films, *ACS Nano* **4**, 2937-2945 (2010).
778 [25] M. Amjadipour, J. MacLeod, J. Lipton-Duffin, A. Tadich, J. J. Boeckl, F. Iacopi, N. Motta,
779 Electron effective attenuation length in epitaxial graphene on SiC, *Nanotechnology*, **30**, 025704
780 (2019).
781 [26] B. Da, Y. Sun, S. F. Mao, Z. M. Zhang, H. Jin, H. Yoshikawa, S. Tanuma, Z. J. Ding, A
782 reverse Monte Carlo method for deriving optical constants of solids from REELS spectra. *J.*
783 *Appl. Phys*. **113**, 214303 (2013).
784 [27] B. Da, H. Shinotsuka, H. Yoshikawa, Z. J. Ding, S. Tanuma, Extended Mermin method for
785 calculating the electron inelastic mean free path. *Phys. Rev. Lett*. **113**, 063201 (2014).

[28] C. J. Tung, Y. F. Chen, C. M. Kwei, T. L. Chou, Differential cross sections for plasmon excitations and reflected electron-energy-loss spectra. *Phys. Rev. B* **49**, 16684 (1994).

[29] H. Venghaus, Redetermination of the dielectric function of graphite. *Phys. Stat. Sol. (b)* **71**, 609-614 (1975).

[30] H. Hibino, H. Kageshima, F. Maeda, M. Nagase, Y. Kobayashi, Y. Kobayashi, H. Yamaguchi, Thickness Determination of Graphene Layers Formed on SiC Using Low-Energy Electron Microscopy, *e-J. Surf. Sci. Nanotechnol.* **6**, 107-110 (2008).

[31] P. Sutter, J. T. Sadowski, E. Sutter, Graphene on Pt(111): growth and substrate interaction, *Phys. Rev. B* **80**, 245411 (2009).

[32] V. U. Nazarov, E. E. Krasovskii, V. M. Silkin, Scattering resonances in two-dimensional crystals with application to graphene, *Phys. Rev. B* **87**, 041405(R) (2013).

[33] L. Frank, E. Mikmeková, I. Müllerová, M. Lejeune, Counting graphene layers with very slow electrons, *Appl. Phys. Lett.*, **106**, 013117 (2015).

[34] S. Srisonphan, M. Kim, and H. K. Kim, Space charge neutralization by electron-transparent suspended graphene, *Sci. Rep.* **4**, 3764 (2014).

[35] A. Kojima, R. Suda, and N. Koshida, Improved quasiballistic electron emission from a nanocrystalline Si cold cathode with a monolayer-graphene surface electrode, *Appl. Phys. Lett.* **112**, 133102 (2018).

[36] B. Da, J. W. Liu, Y. Harada, N. T. Cuong, K. Tsukagoshi, J. Hu, L. H. Yang, Z. J. Ding, H. Yoshikawa, and S. Tanuma, Observation of plasmon energy gain for emitted secondary electron in vacuo. J. Phys. Chem. Lett. **10**, 5770–5775 (2019).

[37] E. Mikmekova, H. Bouyanfif, M. Lejeune, I. Mullerova, M. Hovorka, M. Uncovsky, and L. Frank, Very low energy electron microscopy of graphene flakes, *J. Microsc.* **251**, 123 (2013).

[38] G. Hassink, R. Wanke, I. Rastegar, W. Braun, C. Stephanos, P. Herlinger, J. H. Smet, and J. Mannhart, Transparency of graphene for low-energy electrons measured in a vacuum-triode setup, *APL Mater.* **3**, 076106 (2015).

[39] R. S. Sundaram, M. Steiner, H.-Y. Chiu, M. Engel, A. A. Bol, R. Krupke, M. Burghard, K. Kern, and P. Avouris, The graphene–gold interface and its implications for nanoelectronics. Nano Lett. **11**, 3833 (2011).

[40] J. Tesch, P. Leicht, F. Blumenschein, L. Gragnaniello, M. Fonin, L. E. Marsoner Steinkasserer, B. Paulus, E. Voloshina, and Y. S. Dedkov, Structural and electronic properties of graphene nanoflakes on Au(111) and Ag(111). Sci. Rep. **6**, 23439 (2016).

[41] N. Barrett, E. E. Krasovskii, J.-M. Themlin, V. N. Strocov, Elastic scattering effects in the electron mean free path in a graphite overlayer studied by photoelectron spectroscopy and LEED. *Phys. Rev. B* **71**, 035427 (2005).

[42] Kota Shihommatsu, Junro Takahashi, Yuta Momiuchi, Yudai Hoshi, Hiroki Kato, and Yoshikazu Homma, Formation Mechanism of Secondary Electron Contrast of Graphene Layers on a Metal Substrate, ACS Omega, **2**, 7831–7836 (2017).

[43] M. P. Seah, W. A. Dench, Quantitative electron spectroscopy of surfaces: A standard data base for electron inelastic mean free paths in solids. *Surf. Interface Anal*. **1**, 1-11 (1979).

[44] J. Luo, P. Tian, C. Pan, A. W. Robertson, J. H. Warner, E. W. Hill, G. A. D. Briggs, Ultralow secondary electron emission of graphene. *ACS Nano* **5**, 1047-1055 (2011).

[45] Y. Ueda, Y. Suzuki and K. Watanabe, Secondary-electron emission from multi-layer graphene: time-dependent first-principles study, *Appl. Phys. Express* **11**, 105101 (2018).

[46] I. Miccoli, F. Edler, H. Pfnür, C. Tegenkamp, The 100th anniversary of the four-point probe technique: The role of probe geometries in isotropic and anisotropic systems. *J. Phys.: Condens. Matter* **27**, 223201 (2015).

[47] S. Glass, Handbook *of Infrared Astronomy* (Cambridge University Press, Cambridge, ed. 1, 1999).

[48] E. Runge, E. K. Gross, Density-functional theory for time-dependent systems. *Phys. Rev. Lett*. **52**, 997 (1984).

[49] Z. J. Ding, R. Shimizu, A Monte Carlo modeling of electron interaction with solids including cascade secondary electron production. *Scanning* **18**, 92-113 (1995).

[50] K. Tsubonoya, C. Hu, K. Watanabe, Time-dependent density-functional theory simulation of electron wave-packet scattering with nanoflakes. *Phys. Rev. B* **90**, 035416 (2014).

[51] F. Salvat, A. Jablonski, C. Powell, ELSEPA—Dirac partial-wave calculation of elastic scattering of electrons and positrons by atoms, positive ions and molecules. *Comput. Phys. Commun.* **165**, 157-190 (2005).

[52] P. Blaha, K. Schwarz, G. K. H. Madsen, K. Kvasnicka, J. Luitz, *WIEN2K* (Karlheinz Schwarz, Technische Universitat Wien, Austria, ed. 1, 2001).

[53] S. Tougaard, Inelastic background correction and quantitative surface analysis. *J. Electron Spectrosc. Relat. Phenom*. **52**, 243-271 (1990).

[54] J. F. McClain, J. Sun, K. Pohl, J.-M. Tang, First-principles theory of low-energy electron diffraction and quantum interference in few-layer graphene. arXiv:1311.2917

[55] H. A. Bethe, Zur theorie des durchgangs schneller korpuskularstrahlen durch materie. *Ann. Phys. (Berlin)* **397**, 325-400 (1930) (in German).

[56] P. Hohenberg and W. Kohn, Inhomogeneous Electron Gas. *Phys. Rev.* **136**, B864–B871 (1964).

[57] W. Kohn and L. J. Sham, Self-Consistent Equations Including Exchange and Correlation Effects. *Phys. Rev.* **140**, A1133–A1138 (1965).

[58] P. Giannozzi et al., QUANTUM ESPRESSO: a modular and open-source software project for quantum simulations of materials. *J. Phys.: Condens. Matter* **21**, 395502 (2009).

[59] A. D. Corso, Pseudopotentials periodic table: From H to Pu. *Comput. Mater. Sci.* **95**, 337–350 (2014).

[60] I. Hamada, van der Waals density functional made accurate. *Phys. Rev. B* **89**, 121103 (2014).

[61] H. J. Monkhorst and J. D. Pack, Special points for Brillouin-zone integrations. *Phys. Rev. B* **13**, 5188–5192 (1976).

866

867 **Figures and Tables**

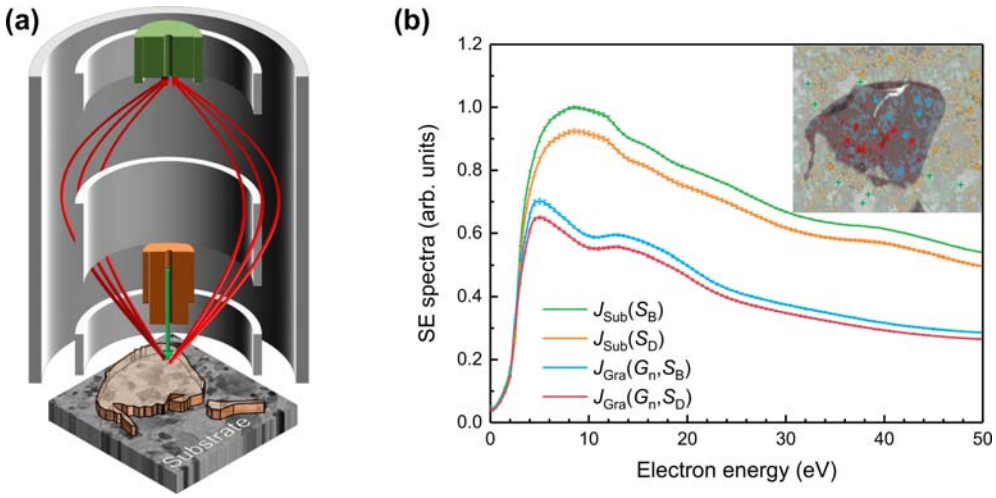

868

869 **Fig. 1** Data collection from substrate-supported graphene samples with different incident
870 measurement sites. **a** Experimental setup for Auger electron spectroscopy, in which graphene
871 flakes were produced on an Au polycrystalline substrate by mechanical exfoliation. **b** Four
872 secondary electron (SE) spectra, $J_{Sub}(S_B)$, $J_{Sub}(S_D)$, $J_{Gra}(G_n, S_B)$, and $J_{Gra}(G_n, S_D)$, were measured
873 at the bright (S_B) and dark (S_D) regions on the bare substrate and bright and dark regions covered
874 by graphene sheets, respectively. The corresponding four regions are marked on the inset
875 scanning electron microscopy image. Each SE spectrum is averaged from eight independent
876 measurements in the energy range from 0 to 50 eV obtained with 0.1-eV energy steps for
877 monolayer graphene on an Au polycrystalline substrate with an incident electron energy of 10
878 keV, and further normalized by the maximum intensity in these spectra. The standard deviations
879 for the eight groups of measurements are presented as error bars at intervals of 0.5 eV. The
880 incident beam positions of the eight groups of measurements are also presented as green diagonal
881 crosses, ochre upright crosses, red diagonal crosses, and azure upright crosses referring to bright
882 and dark regions on the bare substrate and bright and dark regions on the graphene sheets,

respectively. The work function of graphene and that of the bare Au substrate with respect to the cylindrical mirror analyser were used to determine the onset of the spectra.

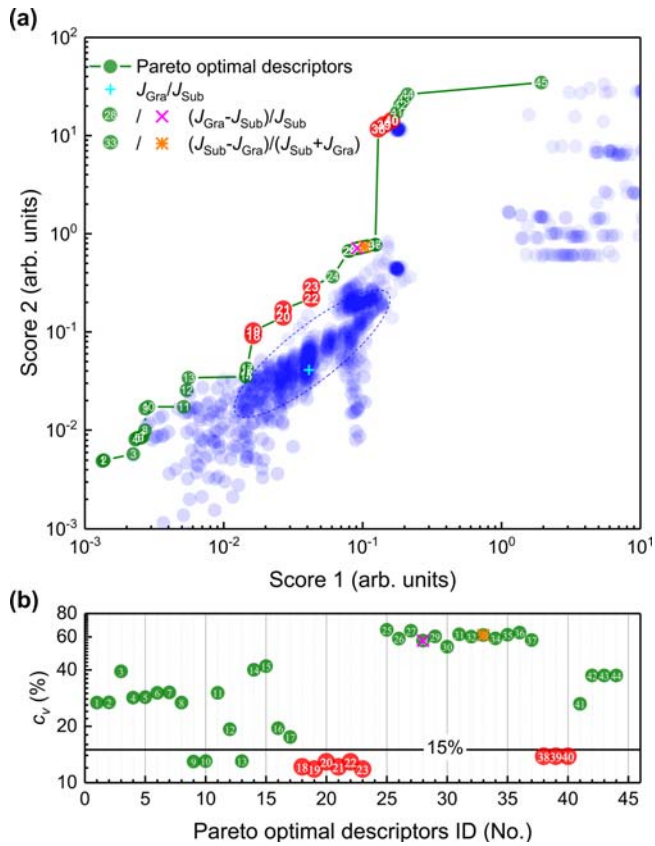

Fig. 2 Identifying principle analytically defined (AD) descriptors from descriptor space. **a** Descriptor performance map, in which the sensitivity to the incident electron energy, E_{in} (Score1), and sensitivity to the layer number of graphene, G_n (Score2), for every candidate descriptor is drawn in this map as x- and y-axes, respectively. The Pareto optimal descriptors (D_n) are highlighted in green and numbered in this descriptor performance map in order of increasing Score1. D_{18}, D_{19}, D_{20}, D_{21} D_{22}, D_{23}, D_{38}, D_{39}, and D_{40}, which can be expressed by Eqn. 2, are highlighted in red with larger labels. The conventional AD descriptor adopted to analysis the SE signals of graphene, i.e. $J_{Gra}(G_n, S_B)/J_{Sub}(S_B)$, $\frac{J_{Gra}(G_n, S_B) - J_{Sub}(S_B)}{J_{Sub}(S_B)}$ [*19*], and $\frac{J_{Sub}(S_B) - J_{Gra}(G_n, S_B)}{J_{Sub}(S_B) + J_{Gra}(G_n, S_B)}$ [*20*], are labelled as cyan crosses, magenta diagonal crosses, and orange

stars. **b** The coefficient of variation (c_v) of Pareto optimal descriptors (D_n) averaged from 600 data points. D_{18}, D_{19}, D_{20}, D_{21} D_{22}, D_{23}, D_{38}, D_{39}, and D_{40} are highlighted in red with larger labels.

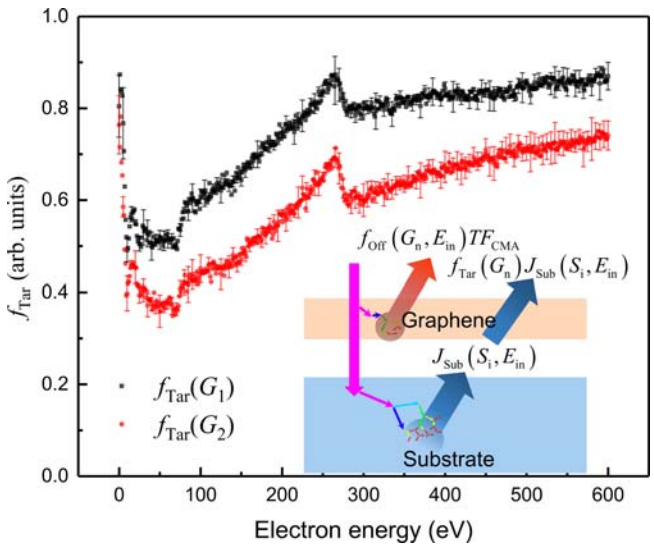

Fig. 3 Target terms determined from the principle descriptors and their physical meaning. The target terms for monolayer graphene $f_{Tar}(G_1)$ and bilayer graphene $f_{Tar}(G_2)$ averaged from incident electron energies of 10, 15, and 20 keV were calculated from the principle descriptors according to Eqn. 5 and are plotted in the energy range of 0–600 eV together with error bars at intervals of 0.5 eV representing one standard deviation. The inset depicts the formation of SE spectra obtained from a substrate-supported graphene sample, in which the SE spectra represent the evolution of a primary electron beam inside a sample driven by the interaction of the sample with moving electrons.

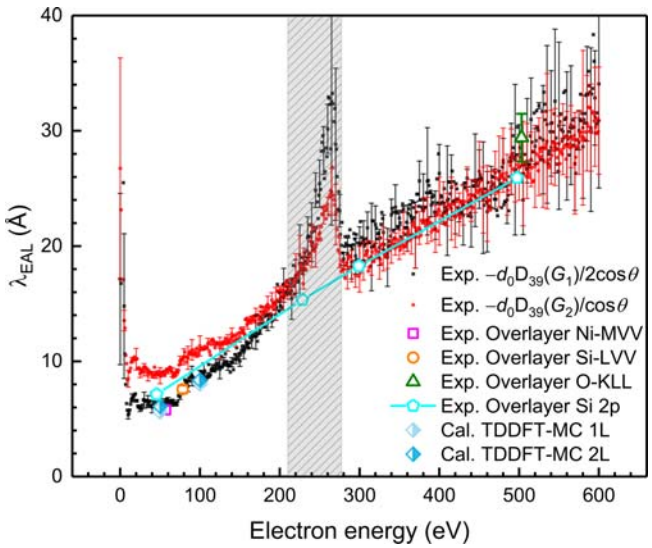

Fig. 4 Effective attenuation lengths (EALs) of graphene. EALs averaged from incident electron energies of 10, 15, and 20 keV for mono- and bilayer graphene using descriptor $D_{39}(G_1)$ and $D_{39}(G_2)$, respectively, and plotted together with error bars at intervals of 0.5 eV representing one standard deviation. EALs for a graphene/Ni sample at 57 eV (Ni MVV spectra) and a graphene/SiO_2 sample at 78 eV (Si LVV spectra) and 503 eV (O KLL spectra) were measured by the overlayer method using AES technique [*24*]. EALs for epitaxial graphene on SiC at 48 eV, 228 eV, 298 eV, and 498 eV, measured by the overlayer method with synchrotron photoelectron spectroscopy [*25*], are also presented. EALs of mono- and bilayer graphene were calculated at 50 and 100 eV by a hybrid method.

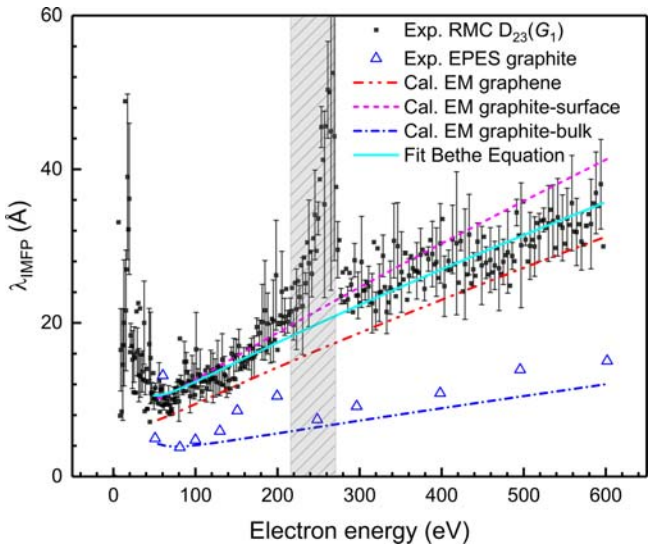

Fig. 5 Inelastic mean free paths (IMFPs) of graphene. IMFPs of monolayer graphene averaged from incident electron energies of 10, 15, and 20 keV determined from descriptor $D_{23}(G_1)$ and plotted together with error bars at intervals of 0.5 eV representing one standard deviation. The IMFPs for monolayer graphene fitted by the Bethe equation [55] at 50–210 and 280–600 eV are plotted as a visual guide (see Appendix F). IMFPs for monolayer graphene, a fictitious graphite surface and bulk graphite above 50 eV were calculated using the extended Mermin (EM) method [*27*]. The IMFP of graphite measured by elastic peak electron spectroscopy [*11*] is also presented.

930

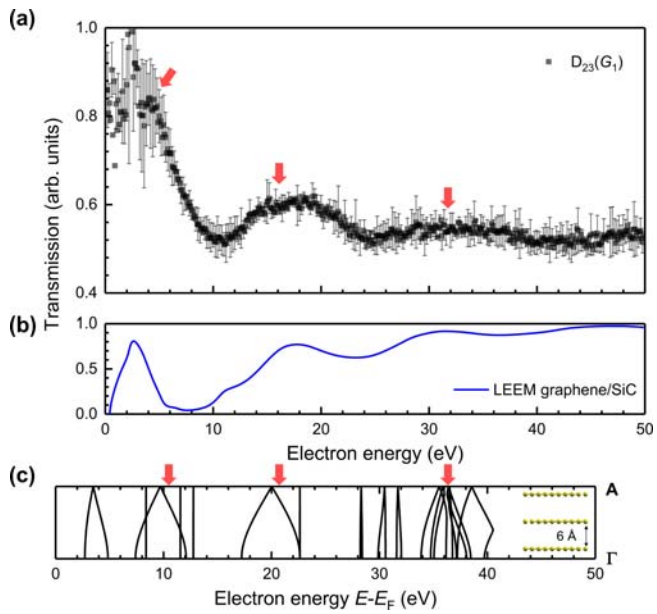

931

932 **Fig. 6** Electron transmission of monolayer graphene. **a** The elastic electron transmission of
933 monolayer graphene [$D_{23}(G_1)$] averaged from 10 keV, 15 keV, and 20 keV primary electron
934 energies, and plotted together with error bars at 0.2-eV intervals representing one standard
935 deviation. **b** Transmission data (T_{LEEM}) estimated from the reflectivity spectra (T_{LEEM} = 1 -
936 R_{LEEM}) obtained from LEEM of a monolayer graphene/SiC sample [*30*]. **c** The electronic band
937 structure of a graphene "pseudo-crystal" in the Γ−A direction determined using first-principles
938 density-functional theory calculations, in which the interlayer distance between graphene sheets
939 was 6 Å. The electronic band structure is plotted referring to the Fermi level, and shifted to lower
940 energy by the work function of graphene (4.6 eV).

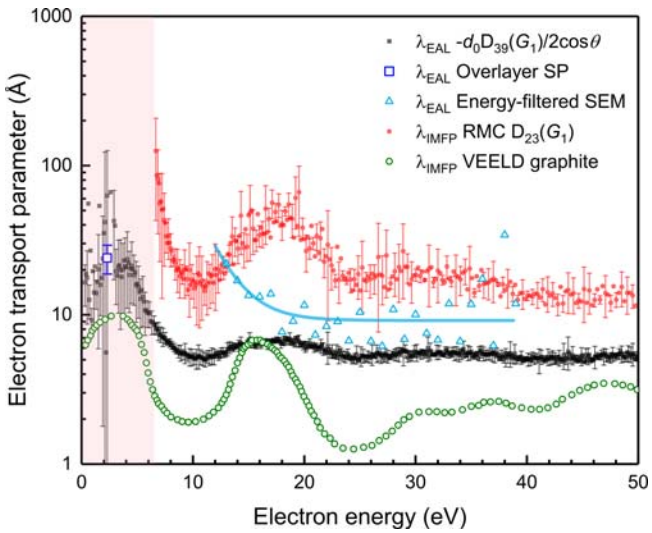

Fig. 7 Low-energy electron transport parameter of monolayer graphene. Effective attenuation length (EAL) and inelastic mean free path (IMFP) for monolayer graphene averaged for incident electron energies of 10, 15, and 20 keV are plotted together with error bars at intervals of 0.2 eV representing one standard deviation. The energy range below 6 eV where the IMFP of monolayer graphene is absent because the elastic scattering cross-section used in the reverse Monte Carlo program cannot be determined is highlighted (pink rectangle) (see Appendix E). The EAL of graphene measured by the overlayer method for graphene/Au at 2.3 eV associated with Au surface plasmons (overlayer SP) is plotted. The IMFP of graphite measured by the very-low-energy electron diffraction technique [*41*] is presented. EALs of a graphene/Ni sample in the energy range of 12–39 eV, measured using energy-filtered scanning electron microscopy [*42*], is presented together with fitted curves as visual guides.

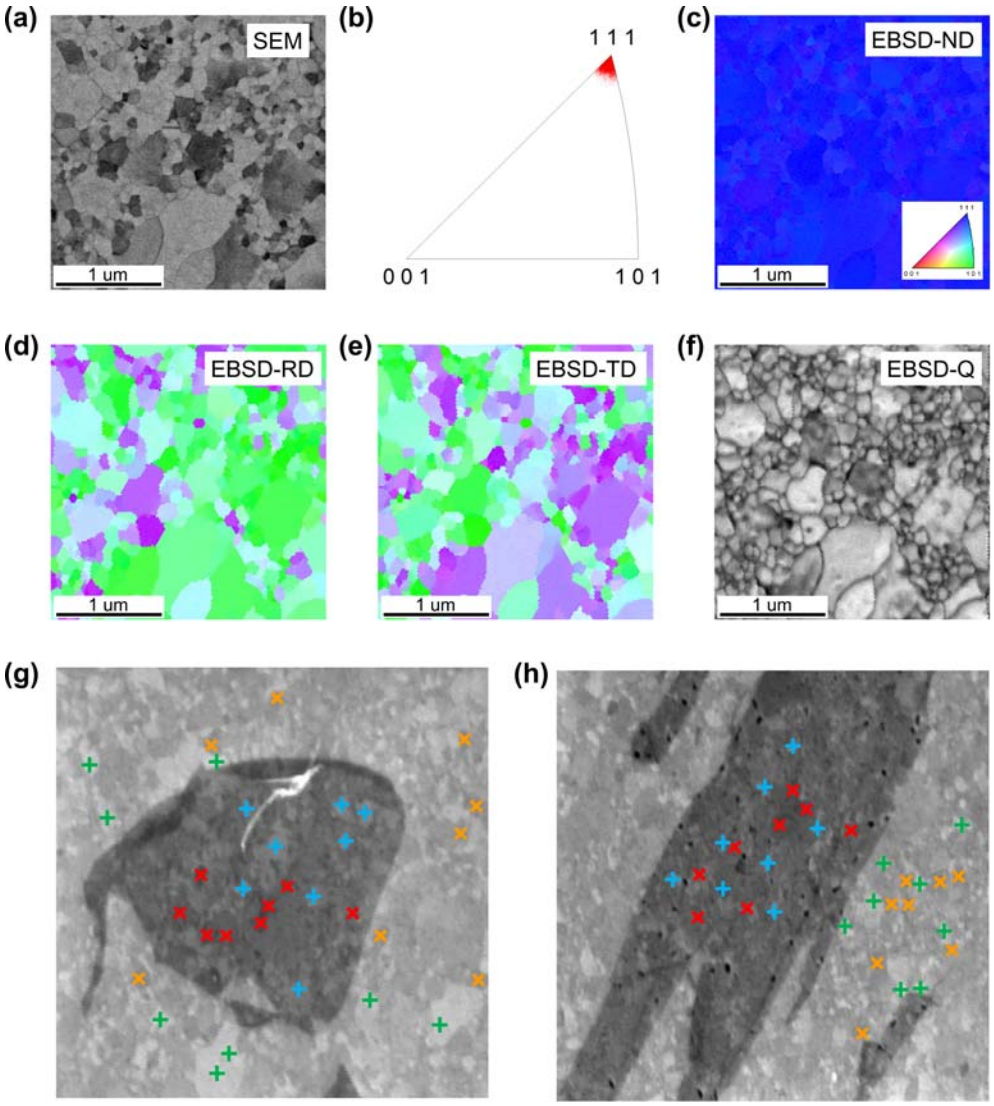

Fig. 8 Electron backscatter diffraction (EBSD) of graphene supported by a polycrystalline Au film substrate. **a**, SEM image of the polycrystalline Au substrate. **b**, Misorientation-axis distributions in ND of the polycrystalline Au sample. EBSD maps for **c**, ND, **d**, rolling direction (RD), **e**, transverse direction (TD), and **f**, EBSD image quality map (EBSD-Q), for the same region of the sample. Reproduced from Ref. [21]. SEM image of **g**, monolayer graphene and **h**, bilayer graphene on a polycrystalline Au substrate. The incident beam positions of the eight groups of measurements are also presented as green diagonal crosses, ochre upright crosses, red

diagonal crosses, and azure upright crosses referring to bright and dark regions on the bare substrate, and bright and dark regions on the graphene sheets, respectively.

964

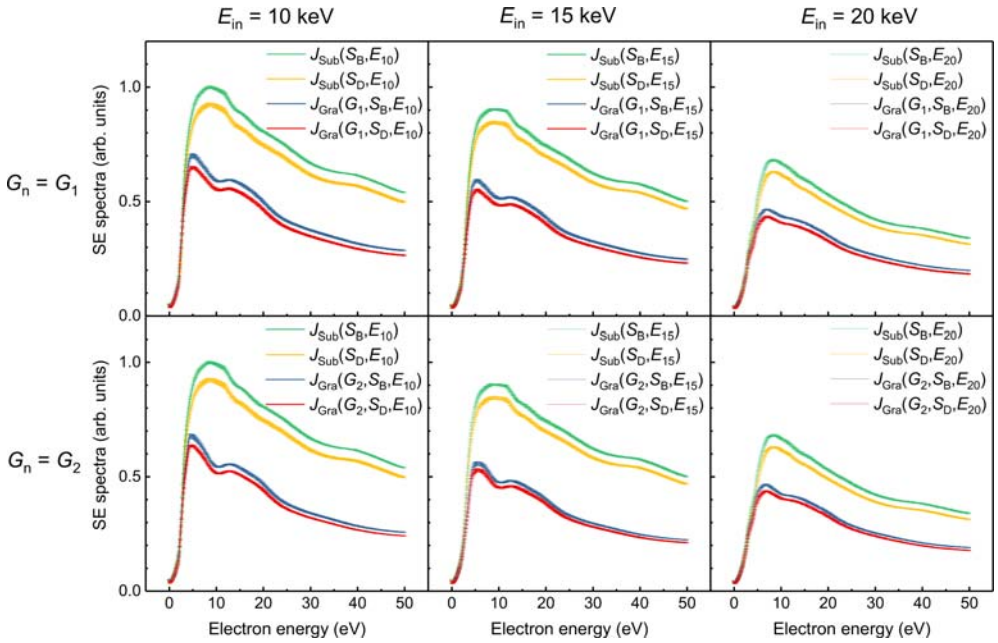

965 **Fig. 9** SE spectra measured in the energy range of 0–50 eV under slightly different conditions.
966 Raw spectra measured in the energy range from 0 to 50 eV with an energy step of 0.1 eV at
967 bright (S_B) and dark regions (S_D) of the Au polycrystalline substrate and similar regions covered
968 by monolayer graphene (G_1) or bilayer graphene (G_2) with incident electron energies of 10 keV
969 (E_{10}), 15 keV (E_{15}), and 20 keV (E_{20}). Spectra are normalized by the maximum intensity of
970 $J_{sub}(S_B, E_{10})$. Each SE spectrum was obtained from eight independent groups of measurements
971 and the standard deviations of these measurements are presented as error bars at intervals of 0.5
972 eV.

973

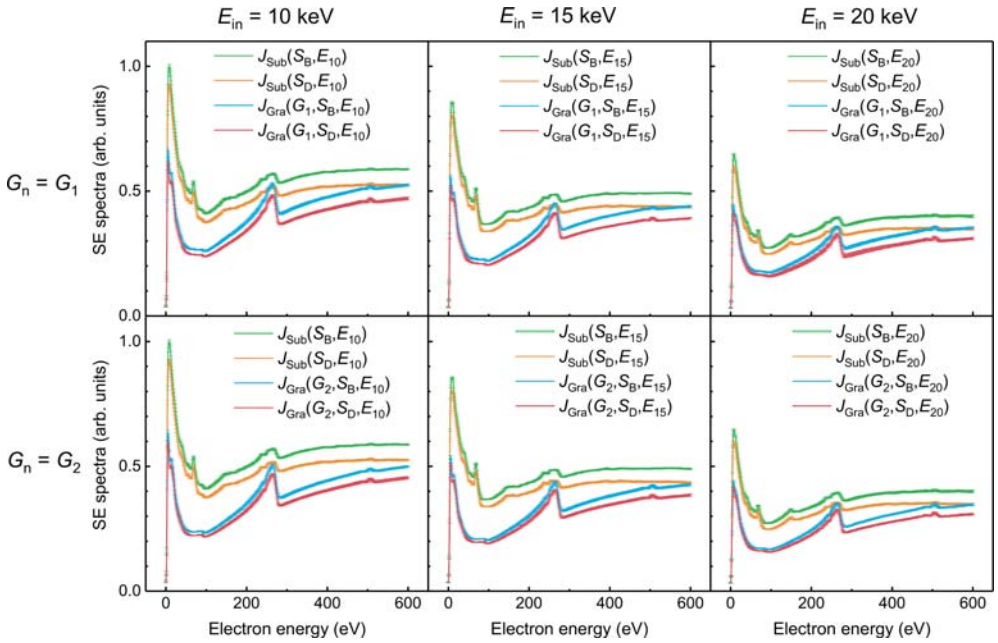

Fig. 10 SE spectra measured in the energy range of 0–600 eV under slightly different conditions. Raw spectra measured in the energy range from 0 to 600 eV with an energy step of 1 eV at bright (S_B) and dark regions (S_D) on a polycrystalline Au substrate and similar regions covered by monolayer graphene (G_1) or bilayer graphene (G_2) with incident electron energies of 10 keV (E_{10}), 15 keV (E_{15}), and 20 keV (E_{20}). Spectra are normalized by the maximum intensity of $J_{sub}(S_B, E_{10})$. Each SE spectrum was obtained from eight independent groups of measurements and the standard deviations of these measurements are presented as error bars at intervals of 5 eV.

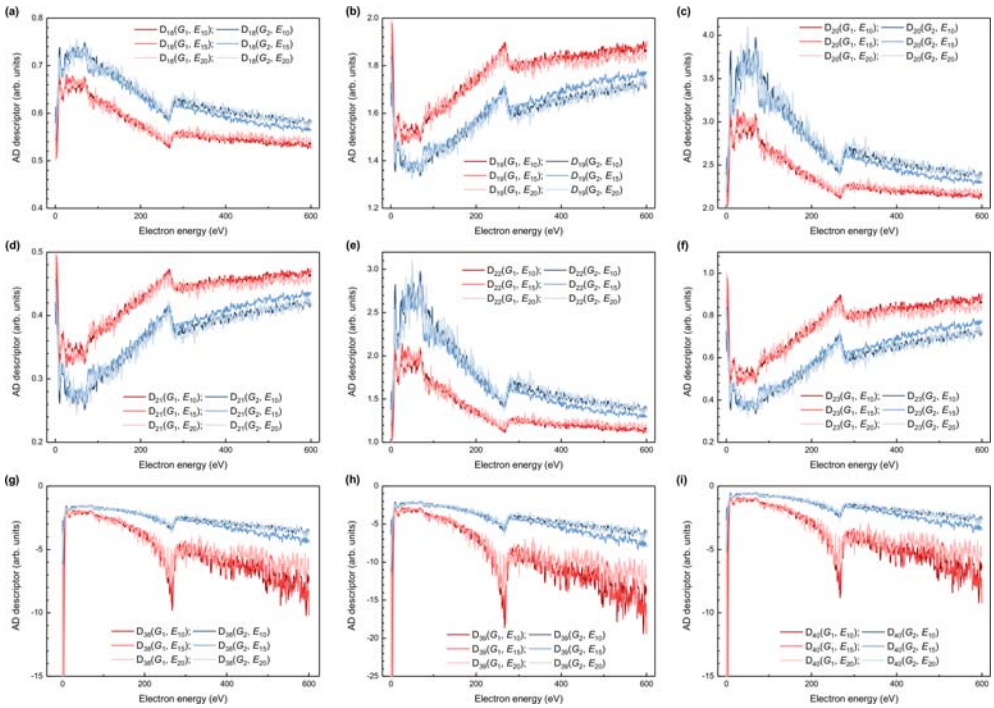

Fig. 11 Nine identified principle descriptors constructed from slightly different measurements. Calculated principle descriptors **a** D_{18}, **b** D_{19}, **c** D_{20}, **d** D_{21}, **e** D_{22}, **f** D_{23}, **g** D_{38}, **h** D_{39}, and **i** D_{40} in the energy range of 0–600 eV for monolayer graphene (G_1) and bilayer graphene (G_2) with incident electron energies of 10 keV (E_{10}), 15 keV (E_{15}), and 20 keV (E_{20}).

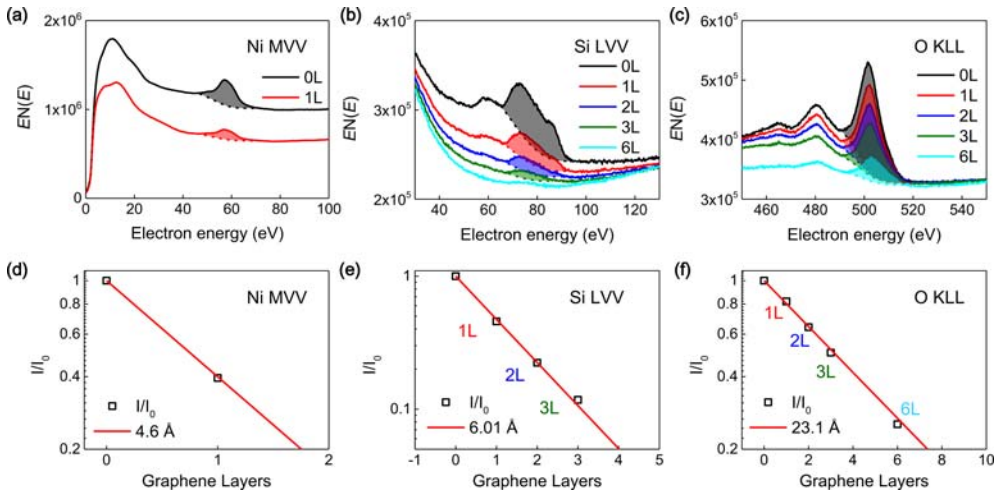

Fig. 12 Measurement of the effective attenuation length for graphene (λ_{EAL}) based on the overlayer method. Plots of **a** Ni MVV spectra taken on a bare Ni substrate and a monolayer of graphene on top of a Ni substrate, and **b** Si LVV and **c** O KLL spectra measured for a bare SiO_2 substrate and one, two, three, and six layers of graphene on top of a SiO_2 substrate. It should be noted that the Auger spectra for the Ni and SiO_2 substrates and monolayer graphene on these substrates are averaged from nine separate measurements from different sample areas. The contributions from Auger electrons are highlighted by coloured bands. Log plots of the **d** Ni MVV, **e** Si LVV, and **f** O KLL spectral intensity attenuation as a function of the number of layers of graphene. The fitting line slope defines $\exp(-G_n d_0/\lambda_{EAL})$, where G_n is the number of graphene sheets and d_0 is the thickness of monolayer graphene (3.35 Å).

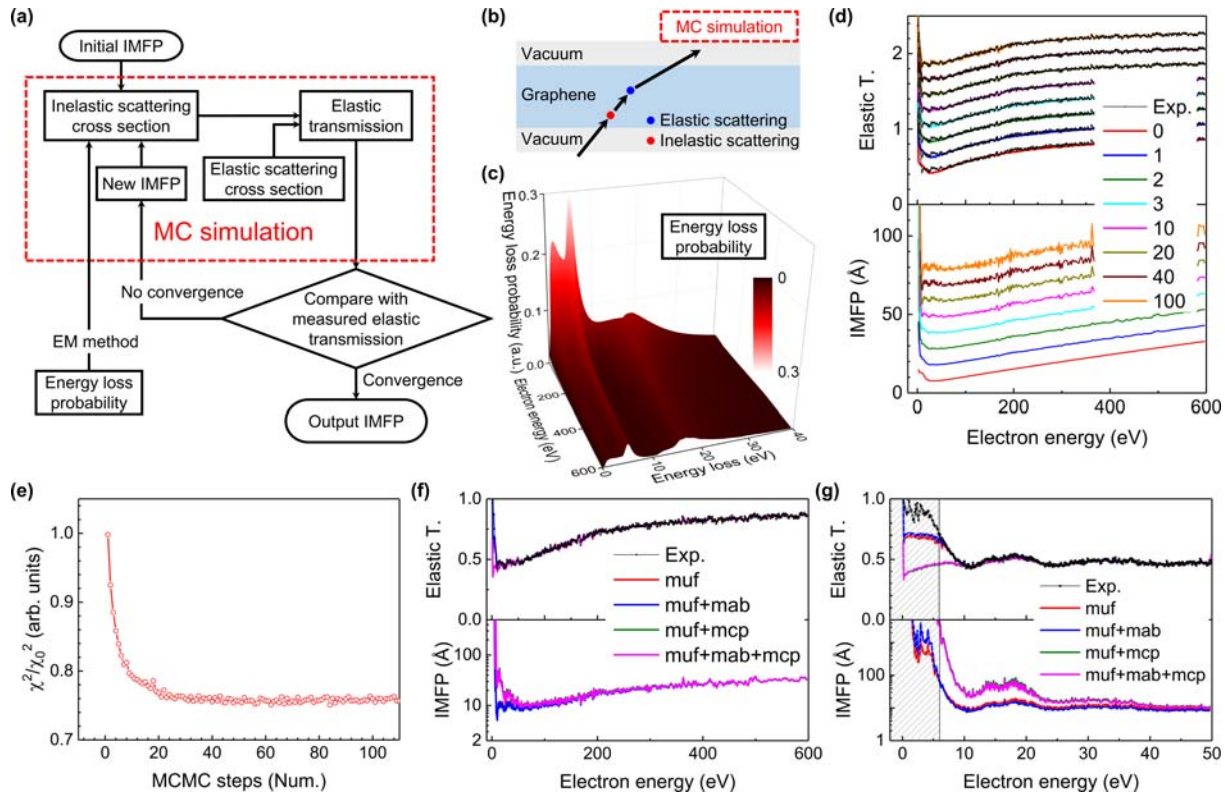

Fig. 13. Reverse Monte Carlo (RMC) program to determine the inelastic mean free path (λ_{IMFP}) of graphene. **a** Flow chart of the RMC program used to extract the λ_{IMFP} of graphene from the measured elastic transmission. **b** Schematic diagram of the conventional MC simulation program, which acts as a single Markov chain Monte Carlo (MCMC) sampling in this RMC method. **c** Energy loss probability calculated based on the dielectric response theory used in this RMC method. **d** Updating process of the simulated elastic transmission (top) and corresponding λ_{IMFP} (bottom) for monolayer graphene in the RMC process. The resulting simulated elastic transmission is compared with experimental measurements for monolayer graphene with an incident electron energy of 10 keV. **e** The normalized least-squares χ_i^2/χ_0^2 for the *i*th MCMC step in the RMC method, where $\chi_i^2 = \sum_j \left\{ \left[I_i^{\mathrm{sim}}(E_j) - I^{\mathrm{exp}}(E_j) \right] / \sigma(E_j) \right\}^2$, wherein the index *j* denotes the *j*th experimental grid values of electron energy *E*, $\sigma(E_j)$ is the weighting factor for accelerating

convergence, I_i^{sim} is the simulated elastic transmission spectrum in the *i*th MCMC step, and I^{exp} is the experimentally measured elastic transmission. The simulated elastic transmission of monolayer graphene and the corresponding λ_{IMFP} after 50 successive MCMC steps are presented in the *E* ranges of **f** 0–600 eV and **g** 0–50 eV based on the different atomic potentials involved in the elastic cross section. These potentials are the muffin-tin potential (muf); muf + absorption potential (muf+mab); muf + correlation-polarization potential (muf+mcp); and muf+mcp+mab; together with the experimentally measured elastic transmission (Exp).

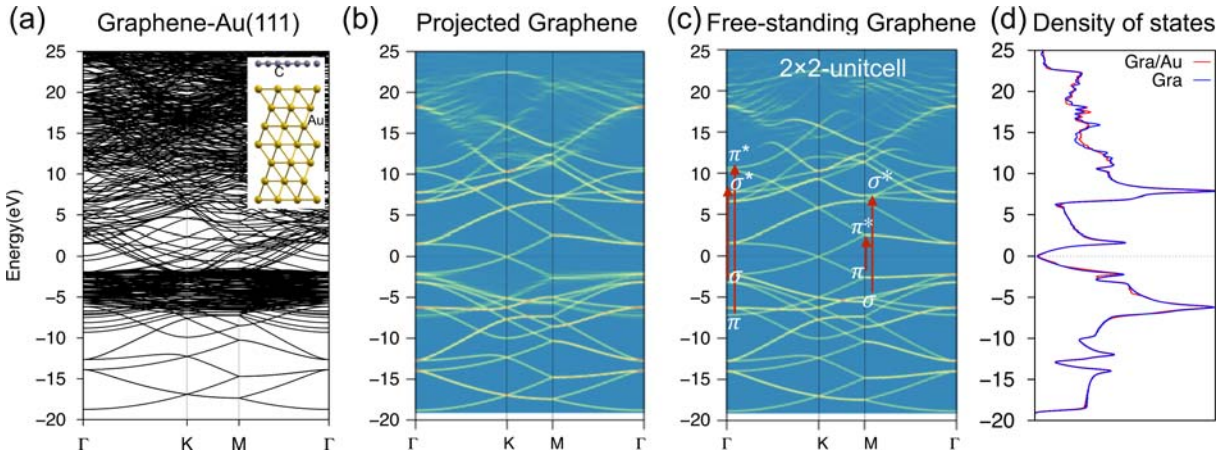

Fig. 14. Electronic structure of a graphene/Au(111) system. **a**, Energy band structure of monolayer graphene on an Au(111) surface. The inset shows the optimized atomic structure of graphene/Au(111), in which the optimized distance between the Au(111) surface and the graphene is 3.4 Å, indicating a weak interaction. The yellow and black balls indicate Au and C atoms, respectively. **b**, The projected energy band of graphene in graphene/Au(111). **c**, Energy band of free-standing monolayer graphene. **d**, Density of states of free-standing graphene and graphene for a graphene/Au(111) surface. The Fermi energy level is set at 0.0 eV.

Table 1. Weight factors **a** of Pareto optimal descriptors. Expressions describing weight factor **a** are provided in Eq. 1 in the main text.

Pareto optimal Descriptor	Weight factor **a**	Pareto optimal Descriptor	Weight factor **a**
D_1	[−1, −1, −1, 1, 0, −1, −1, 0]	D_{24}	[0, −1, 0, 1, 0, −1, 1, 0]
D_2	[−1, 0, 0, −1, −1, −1, −1, −1]	D_{25}	[0, −1, 0, 1, −1, 0, 1, 1]
D_3	[−1, 0, −1, 1, 0, −1, −1, −1]	D_{26}	[0, −1, 0, 1, 0, −1, 1, 1]
D_4	[−1, 1, −1, −1, 0, 0, −1, 0]	D_{27}	[0, −1, 0, 1, −1, 1, 0, 1]
D_5	[−1, 1, 0, −1, −1, 1, −1, −1]	D_{28}	[0, −1, 0, 1, 0, 0, 0, −1]
D_6	[−1, 1, 1, 1, −1, 1, 1, 0]	D_{29}	[0, −1, 0, 1, 0, 0, −1, −1]
D_7	[0, 0, 0, −1, −1, 1, 1, 1]	D_{30}	[0, −1, 0, 1, −1, 1, 0, −1]
D_8	[−1, 0, 0, −1, 0, −1, −1, 0]	D_{31}	[0, −1, 0, 1, 0, −1, −1, −1]
D_9	[−1, 0, 0, −1, −1, −1, −1, −1]	D_{32}	[0, −1, 0, 1, −1, 0, −1, −1]
D_{10}	[0, 0, −1, −1, −1, 1, 1, 0]	D_{33}	[0, −1, 0, 1, 0, −1, 0, −1]
D_{11}	[0, 0, 0, −1, −1, 1, 1, 0]	D_{34}	[0, −1, 0, 1, −1, 0, 0, −1]
D_{12}	[−1, 1, −1, −1, −1, 1, 1, 0]	D_{35}	[0, −1, 0, 1, −1, −1, 0, −1]
D_{13}	[−1, 1, 0, −1, −1, 1, 1, 0]	D_{36}	[0, −1, 0, 1, −1, −1, 1, −1]
D_{14}	[−1, 1, 0, 1, −1, 1, 0, −1]	D_{37}	[0, −1, 0, 1, −1, 0, 1, −1]
D_{15}	[−1, 1, 0, −1, −1, 1, 0, 1]	D_{38}	[0, 0, −1, 1, −1, 1, 1, −1]
D_{16}	[−1, 1, 1, 0, −1, 0, 0, −1]	D_{39}	[−1, 1, −1, 1, −1, 1, 1, −1]
D_{17}	[−1, 0, 0, −1, −1, 1, 1, 0]	D_{40}	[−1, 1, 0, 0, −1, 1, 1, −1]
D_{18}	[0, 0, −1, 1, −1, 1, −1, 1]	D_{41}	[0, −1, 1, 0, −1, 1, 1, −1]
D_{19}	[−1, 1, −1, 1, 0, 0, −1, 1]	D_{42}	[−1, 0, 1, 0, −1, 1, 1, −1]
D_{20}	[−1, 1, −1, 1, −1, 1, 0, 0]	D_{43}	[−1, −1, 1, 1, −1, 1, 1, −1]
D_{21}	[−1, 1, 0, 0, −1, 1, −1, 1]	D_{44}	[0, −1, 0, 1, −1, 1, 1, −1]
D_{22}	[0, 0, −1, 1, −1, 1, 0, 0]	D_{45}	[−1, −1, 0, 1, −1, −1, 1, 0]
D_{23}	[−1, 1, 0, 0, 0, 0, −1, 1]		

Table 2. Weight factors (**a** and **b**) of principle descriptors. Expressions describing weight factor **a** and **b** are provided in Eqs. (1,2), respectively.

Principle descriptor	Weight factor **a**	Weight factor **b**
D_{18}	[0, 0, −1, 1, −1, 1, −1, 1]	[0, −1, −1, −1]
D_{19}	[−1, 1, −1, 1, 0, 0, −1, 1]	[−1, −1, 0, −1]
D_{20}	[−1, 1, −1, 1, −1, 1, 0, 0]	[−1, −1, −1, 0]
D_{21}	[−1, 1, 0, 0, −1, 1, −1, 1]	[−1, 0, −1, −1]
D_{22}	[0, 0, −1, 1, −1, 1, 0, 0]	[0, −1, −1, 0]
D_{23}	[−1, 1, 0, 0, 0, 0, −1, 1]	[−1, 0, 0, −1]
D_{38}	[0, 0, −1, 1, −1, 1, 1, −1]	[0, −1, −1, 1]
D_{39}	[−1, 1, −1, 1, −1, 1, 1, −1]	[−1, −1, −1, 1]
D_{40}	[−1, 1, 0, 0, −1, 1, 1, −1]	[−1, 0, −1, 1]

1041